Shear thickening, frictionless and frictional rheologies

Romain Mari,[1] Ryohei Seto,[1] Jeffrey F. Morris,[1,2] and Morton M. Denn[1,2]

[1]*Benjamin Levich Institute, City College of New York, New York, NY 10031, USA*

[2]*Department of Chemical Engineering, City College of New York, New York, NY 10031, USA*

(Dated: April 3, 2014)

arXiv:1403.6793v2 [cond-mat.soft] 2 Apr 2014

Abstract

Particles suspended in a Newtonian fluid raise the viscosity and also generally give rise to a shear-rate dependent rheology. In particular, pronounced shear thickening may be observed at large solid volume fractions. In a recent article (R. Seto, R. Mari, J. F. Morris, and M. M. Denn., Phys. Rev. Lett., 111:218301, 2013) we have considered the minimum set of components to reproduce the experimentally observed shear thickening behavior, including Discontinuous Shear Thickening (DST). We have found frictional contact forces to be essential, and were able to reproduce the experimental behavior by a simulation including this physical ingredient along with viscous lubrication. In the present article, we thoroughly investigate the effect of friction and express it in the framework of the jamming transition. The viscosity divergence at the jamming transition has been a well known phenomenon in suspension rheology, as reflected in many empirical laws for the viscosity. Friction can affect this divergence, and in particular the jamming packing fraction is reduced if particles are frictional. Within the physical description proposed here, shear thickening is a direct consequence of this effect: as the shear rate increases, friction is increasingly incorporated as more contacts form, leading to a transition from a mostly frictionless to a mostly frictional rheology. This result is significant because it shifts the emphasis from lubrication hydrodynamics and detailed microscopic interactions to geometry and steric constraints close to the jamming transition.

I. INTRODUCTION

A. Shear thickening

Suspensions (solid particles immersed in a fluid) exhibit a wide range of rheological behaviors, including shear thinning, shear thickening, and finite normal stress differences. Shear thickening [Barnes 1989, Brown and Jaeger 2014], where the viscosity increases with shear rate even if the suspending fluid is Newtonian, is a particularly intriguing phenomenon. In the extreme case of Discontinuous Shear Thickening (DST; for early descriptions see the work of Williamson [1930], Williamson and Hecker [1931], Freundlich and Roder [1938]), which is observed at high volume fractions of solid material, the viscosity can increase by several orders of magnitude at a critical shear rate.

The variety of systems showing a DST suggests that this may be a universal behavior that is obtained with a minimum set of physical ingredients. Even though most of the data available are for Brownian suspensions (that is, sub-micrometer particles) [Fagan and Zukoski 1997, Boersma *et al.* 1990, Hoffman 1972, D'Haene *et al.* 1993, O'Brien and Mackay 2000, Metzner and Whitlock 1958, Bender and Wagner 1995, 1996, Maranzano and Wagner 2001a,b, 2002, Frith *et al.* 1996], thermal motion does not seem necessary to observe DST, as experiments with micrometer scale [Boersma *et al.* 1990, Lootens *et al.* 2004, 2005, Larsen *et al.* 2010] or larger particles [Freundlich and Roder 1938, Bertrand *et al.* 2002, Brown and Jaeger 2009, 2012, Fall *et al.* 2010] show. Inertia has also been associated with the existence of shear thickening in suspensions [Fall *et al.* 2010, Lemaître *et al.* 2009, Trulsson *et al.* 2012, Fernandez *et al.* 2013], based on the initial ideas of Bagnold [1954], but the Bagnoldian scaling of a viscosity proportional to the shear rate is clearly milder than the abrupt shear thickening observed in experiments. Moreover the particle Reynolds numbers probed by rheometric flows are too small for inertia to be a factor in DST.

Indeed, the apparently simple experimental system of nearly rigid non-Brownian neutrally buoyant particles immersed in a Newtonian fluid exhibits DST in the Stokes regime [Brown and Jaeger 2009, 2012], indicating that the phenomenon stems from a rather restricted set of simple ingredients. The puzzle has very few pieces. In the Stokes regime, however, non-Brownian neutrally buoyant hard spheres in a Newtonian fluid will create a suspension whose rheology is independent of shear rate, as there is only one force scale, the hydrodynamic one. So there cannot be *too few* pieces.

B. Fluid mechanics and granular physics perspectives

The flow of suspensions has historically been studied from a fluid mechanics perspective, and the emphasis has been on a description based on hydrodynamic interactions. Suspensions are usually described as hard particles immersed in a Newtonian fluid, interacting through hydrodynamics (including Brownian forces) and sometimes an additional soft repulsive potential (approximating an electric double-layer or mimicking polymer coating, for instance). They are typically studied in the Stokes flow regime, at vanishing particle Reynolds number $Re \equiv \rho_0 a^2 \dot{\gamma}/\eta_0$, and Stokes number $St \equiv \rho a^2 \dot{\gamma}/\eta_0$ (with $\dot{\gamma}$ the shear rate; ρ_0 and η_0 the density and viscosity of the fluid phase, respectively; and ρ and a the density and size of the solid particles, respectively). The key point is that the hard cores of the particles are treated as boundary conditions for the Stokes equations that describe the fluid phase; the particles never directly generate forces through contacts. This treatment is

self-consistently justified by the fact that the Stokes flow between two rigid surfaces leads to a lubrication force whose resistance coefficient diverges at contact, effectively preventing two particles from colliding. Within this framework, shear thickening is explained by the creation at large shear rates of dense clusters of particles (*hydro-clusters*), which are highly dissipative due to the singular lubrication flows between the particles [Bender and Wagner 1996, Brady and Bossis 1985, Melrose and Ball 2004a, Wagner and Brady 2009]. While this purely fluid mechanical point of view is able to describe the flow and rheology of moderately dense suspensions, it seems unable to explain the abrupt shear thickening observed in dense suspensions. Simulations by Stokesian Dynamics give a weak logarithmic shear thickening [Brady and Bossis 1988, Bossis and Brady 1989, Phung *et al.* 1996, Foss and Brady 2000, Melrose and Ball 2004b], thereby raising the issue of the validity of this approach at high volume fractions.

In the past few years, new ideas have emerged from the granular rheology perspective. Boyer *et al.* [2011] developed an analogy between the rheology of suspensions and the rheology of granular materials. In dry granular flow, the rheology depends on the ratio between inertia and particle pressure [Deboeuf *et al.* 2009]: if the inertia dominates, particles bounce around and the stresses are essentially due to momentum transport based on collisions (the granular gas regime), whereas if the pressure dominates, particles are forced to stay at contact and the stresses are dominated by contact force chains (the granular packing regime). This perspective can be incorporated in a dimensionless *inertial number* $I \equiv \dot{\gamma} d \sqrt{\rho/\Pi}$ [da Cruz *et al.* 2005], where d is the diameter of the solid particles, ρ their density, and Π the particle pressure. Similarly, for suspensions in the Stokes regime there is a *viscous number* $I_\mathrm{v} \equiv \eta_0 \dot{\gamma}/\Pi$, where η_0 is the viscosity of the suspending fluid, which compares viscous dissipation to the particle pressure [Boyer *et al.* 2011]. The stresses can be dominated either by viscous dissipation if $I_\mathrm{v} \gg 1$ (when particles are far apart) or by a contact network if $I_\mathrm{v} \ll 1$. This results in constitutive laws for the viscosity and other stress components and for the volume fraction that are unique functions of I_v. One can anticipate that the regimes $I \ll 1$ and $I_\mathrm{v} \ll 1$, both of which are dominated by the approach to the jamming transition, will share some similarities. Indeed, they do share a power-law scaling (typical of the jamming transition) between particle pressure and distance to the jamming point $\Pi \sim (\phi_\mathrm{J} - \phi)^{-2}$ [Boyer *et al.* 2011, Forterre and Pouliquen 2008]. The scaling is the same for the other stress components, including the important case of shear stress $\sigma \sim (\phi_\mathrm{J} - \phi)^{-2}$. These power laws are now understood to represent a universal behavior close to jamming [Lerner *et al.* 2012]. With these ideas, the emphasis has shifted from hydrodynamics and detailed microscopic interactions to geometry and steric constraints close to the jamming transition.

While those new ideas have proven to be successful in explaining some of the rheology at high volume fractions [Trulsson *et al.* 2012, Boyer *et al.* 2011, Lerner *et al.* 2012], they cannot account for non-Newtonian behavior in the Stokes regime. The case of DST is particularly puzzling: whereas intuition suggests that DST is a manifestation of jamming [Bertrand *et al.* 2002, Brown and Jaeger 2009, Cates *et al.* 1998, Lootens *et al.* 2003, Hébraud and Lootens 2005], DST is not captured by the I_v-based rheology, which predicts no shear rate dependence in the Stokes regime [Trulsson *et al.* 2012, Lerner *et al.* 2012], and reduces to a ϕ-dependent rheology [Boyer *et al.* 2011]. Simply stated, this rheology predicts the correct volume fraction dependence of the viscosity at fixed shear rate, but completely fails at predicting the shear rate dependence at fixed volume fraction.

C. This work

In this article, which extends and complements a previous publication [Seto *et al.* 2013], we show how jamming is related to shear thickening and how to escape the apparent contradiction described above. The starting point is to note that the jamming transition, while it exhibits some universal features that are independent of the microscopic interactions like the scalings described above, retains a clear signature of the microscopic details in the volume fraction at which it occurs. For instance, it is well known that jamming can occur anywhere between $\phi_{\mathrm{J}}^{\mu=\infty} \approx 0.55$ and $\phi_{\mathrm{J}}^{\mu=0} \approx 0.64$ depending on the friction coefficient μ between the grains [Song *et al.* 2008]. This means that the relation $\phi(I_{\mathrm{v}})$ actually depends on μ, which in turn implies that $\eta(\phi)$ depends on μ. Therefore, if there exists a mechanism such that μ (or an effective friction coefficient) varies with the shear rate $\dot{\gamma}$, one can obtain a non-Newtonian rheology within the framework of Boyer *et al.* [2011].

We introduced such a mechanism in a recent article [Seto *et al.* 2013], and here we thoroughly explore its consequences through numerical simulations of dense non-Brownian suspensions under simple shear flow. We note that two other recent papers have independently introduced similar but somewhat different mechanisms to achieve a rate-dependent friction coefficient $\mu(\dot{\gamma})$ in simple shear flow simulations [Fernandez *et al.* 2013, Heussinger 2013].

The present work shows the importance of frictional contacts in dense suspension rheology. Of course, particles must form contacts during flow in order for the rheology to depend on the friction coefficient, and here we come up against one assumption of the fluid mechanics perspective. In fact, it is known that particles do come in contact under flow, even in the dilute limit, perhaps due to surface roughness [Lootens *et al.* 2005, Davis 1992, Zhao and Davis 2002, Blanc *et al.* 2011]. One simply has to accept that those contacts, though not essential to the rheology of dilute or semi-dilute suspensions (as the successes of Stokesian Dynamics demonstrate), become important at large volume fractions. But contacts are a necessity if one thinks of the large volume-fraction limit of jamming ($I_{\mathrm{v}} \to 0$): there is no more room in this limit for lubrication films between particles, and contacts must proliferate and dominate the rheology. Besides enforcing the geometric constraint of no overlapping particles, those contacts bring a new restriction to reorganization at the microscopic level: they carry significant tangential forces due to friction. It is worth noting that even though the close-range hydrodynamics (i.e., lubrication forces) also generate some tangential forces, they are of a fundamentally different nature. For a relative motion between two nearby particles, the normal lubrication force diverges as the inverse of the interparticle gap, whereas the tangential lubrication force diverges only logarithmically with vanishing gap, which means that the effective friction coefficient vanishes in the limit of a small gap. Thus lubrication, as in its literal meaning, provides very little resistance to relative tangential motion compared to relative normal motion. This stands in contrast to the frictional contact forces, for which the friction coefficient is finite; i.e., tangential and normal contact forces are of comparable order. It follows that the constraint introduced by contact friction is much more efficient at increasing the viscosity than is lubrication.

Describing the physics of contact and motion when the gap between two particles in a suspension is smaller than, say, 1 nm, is not an easy task. Moreover, one cannot expect to find generic behavior, as interactions will vary depending on the nature of the solid particles and of the suspending fluid. However, this level of detail may not be essential to understanding the physics that emerges at a macroscopic level. At high volume fractions

it is reasonable to expect that the universality associated with the jamming singularity will dominate the rheology of suspensions. Our approach in this work is thus to study the rheology of minimal model systems that include hydrodynamics, a repulsive interaction, and frictional contacts between particles. These interactions, while being realistic, will be simplified to their essence.

II. MODELS AND METHODS

A. Merging hydrodynamic interactions and granular contact models

1. *Equations of motion*

In a suspension, the flow of the fluid is described by the Cauchy momentum equation (the Navier-Stokes equation if the fluid is Newtonian), while the motion of the particles is given by Newton's equation of motion:

$$\boldsymbol{m} \cdot \frac{\mathrm{d}}{\mathrm{d}t} \begin{pmatrix} \boldsymbol{U} \\ \boldsymbol{\Omega} \end{pmatrix} = \sum_{\alpha} \begin{pmatrix} \boldsymbol{F}_{\alpha}(\boldsymbol{U}, \boldsymbol{\Omega}, \boldsymbol{r}) \\ \boldsymbol{T}_{\alpha}(\boldsymbol{U}, \boldsymbol{\Omega}, \boldsymbol{r}) \end{pmatrix}, \tag{1}$$

where $\boldsymbol{m}$ is the mass/moment-of-inertia matrix, $\boldsymbol{U}$ and $\boldsymbol{\Omega}$ are the translational and rotational velocity vectors, and $\boldsymbol{F}_{\alpha}$ and $\boldsymbol{T}_{\alpha}$ are the force and torque vectors, respectively. The right-hand side consists of two different types of forces: some depend only on the configurations $\boldsymbol{r}$ of the particles (e.g., forces derived from a potential), but some also depend on the velocities $\boldsymbol{U}$ and $\boldsymbol{\Omega}$, including inelastic contact forces (e.g., contacts with dashpot terms) and fluid-particle interactions (hydrodynamic interactions).

We will study the rheology of this suspension under an imposed simple shear flow field $\boldsymbol{U}^{\infty}(\boldsymbol{r})$ expressed using the vorticity $\boldsymbol{\Omega}^{\infty}$ and the rate-of-strain tensor $\boldsymbol{E}^{\infty}$ as

$$\boldsymbol{U}^{\infty}(\boldsymbol{r}) = \boldsymbol{\Omega}^{\infty} \times \boldsymbol{r} + \boldsymbol{E}^{\infty} \cdot \boldsymbol{r}. \tag{2}$$

At a shear rate $\dot{\gamma}$, a simple shear flow corresponds to the following nonzero elements: $\Omega_2^{\infty} = \dot{\gamma}/2$ and $E_{12}^{\infty} = E_{21}^{\infty} = \dot{\gamma}/2$.

In many experimental flows, including the ones for which shear thickening is typically observed, the particle Reynolds number and the Stokes number are very small due to the small size of the suspended particles. This means that the equation of motion for the particles can be studied in its overdamped limit, which is simply a quasi-static force balance equation. As will be detailed in sections II A 2, II A 3 and II B below, in this regime the velocity dependence coming from the hydrodynamic interactions and the contact forces has a linear form, and the force balance equation can be written as a linear algebraic relation having the form

$$\boldsymbol{0} = \boldsymbol{R} \cdot \begin{pmatrix} \boldsymbol{U} - \boldsymbol{U}^{\infty} \\ \boldsymbol{\Omega} - \boldsymbol{\Omega}^{\infty} \end{pmatrix} + \begin{pmatrix} \boldsymbol{F}(\boldsymbol{r}) \\ \boldsymbol{T}(\boldsymbol{r}) \end{pmatrix}, \tag{3}$$

Therefore, our simulation of a suspension under a simple shear flow in the Stokes regime requires solving eq. (3) for the velocities, and obtaining the positions $\boldsymbol{r}$ of the particles at any time t through time integration of these velocities.

2. Hydrodynamic interactions

In principle, hydrodynamic interactions can be determined by solving the Stokes equations, but this is extremely expensive from a computational view point. For dense suspensions, however, the dominant hydrodynamic interactions come from the fluid flow in the narrow gaps between nearby solid particles [Ball and Melrose 1997], because those flows become singular (with diverging gradients) when the gaps are vanishingly small. They give rise to pair-wise short range lubrication forces (as opposed to the many-body nature of the full, long-range hydrodynamic interactions). As a consequence, the linear relations between velocities and hydrodynamic forces simply contain a contribution from the Stokes drag and a contribution from the lubrication:

$$\begin{pmatrix} \boldsymbol{F}_{\mathrm{H}} \\ \boldsymbol{T}_{\mathrm{H}} \end{pmatrix} = -\big(\boldsymbol{R}_{\mathrm{Stokes}} + \boldsymbol{R}_{\mathrm{Lub}}\big) \cdot \begin{pmatrix} \boldsymbol{U} - \boldsymbol{U}^{\infty} \\ \boldsymbol{\Omega} - \boldsymbol{\Omega}^{\infty} \end{pmatrix} + \boldsymbol{R}'_{\mathrm{Lub}} : \boldsymbol{E}^{\infty}. \tag{4}$$

$\boldsymbol{R}_{\mathrm{Stokes}}$ is a diagonal matrix giving Stokes drag forces and torques, and $\boldsymbol{R}_{\mathrm{Lub}}$ and $\boldsymbol{R}'_{\mathrm{Lub}}$ are sparse matrices [Ball and Melrose 1997].

Consistent with our choice of keeping only physically relevant near-distance interactions, we use only the leading terms for the resistance matrices. Physically, the terms included in our model correspond to the squeeze, shear, and pump modes of Ball and Melrose [1997] (we do not consider their twist mode, as it is not associated with a divergence of the resistance at contact, and is thus subdominant). Defining the non-dimensional gap $h^{(i,j)}$ between particles i and j having radii a_i and a_j as $h^{(i,j)} \equiv 2(r^{(i,j)} - a_i - a_j)/(a_i + a_j)$ and the center-to-center unit vector $\boldsymbol{n}_{ij} \equiv (\boldsymbol{r}^{(j)} - \boldsymbol{r}^{(i)})/r^{(i,j)}$ with $r^{(i,j)} = |\boldsymbol{r}^{(j)} - \boldsymbol{r}^{(i)}|$, the modes associated with relative displacements respectively along and tangential to $\boldsymbol{n}_{ij}$ have singular behaviors with leading terms diverging as $1/h^{(i,j)}$ and $\log(1/h^{(i,j)})$ [Jeffrey and Onishi 1984, Jeffrey 1992]. The consequence of the singularity in the squeeze mode (i.e., along $\boldsymbol{n}_{ij}$) is that there should not be any contact between particles [Ball and Melrose 1995]. However, as mentioned in the introduction, this statement is only true for perfectly idealized situations, and not realistic even for model experimental systems consisting of spherical particles due to, for example, a finite surface roughness [Lootens *et al.* 2005, Davis 1992, Zhao and Davis 2002, Blanc *et al.* 2011] or a breakdown of the continuity assumption for the fluid at the molecular mean free path scale [Ho and Tai 1998]. In order to mimic this reality, we regularize the singularities arising in the lubrication resistances by inserting a small cutoff length scale δ [Trulsson *et al.* 2012], which can be thought of as the length scale of the particle surface roughness; the leading terms we use for normal and tangential displacements then behave as $1/(h^{(i,j)} + \delta)$ and $\log(1/(h^{(i,j)} + \delta))$. In the simulations, we set $\delta = 10^{-3}a$, giving large enough resistance for the squeeze mode compared to the typical hydrodynamic force. The detailed expressions for the resistance matrices $\boldsymbol{R}_{\mathrm{Lub}}$ and $\boldsymbol{R}'_{\mathrm{Lub}}$ are given in Appendix A.

3. Contact model

There are several models that one can use to describe frictional contacts between particles. We use a stick/slide friction model employing springs and dashpots that is commonly used in granular physics [Cundall and Strack 1979, Luding 2008]. The normal and tangential

components of the force and the torque for particles having radii a_i and a_j are obtained as

$$\begin{aligned}
\boldsymbol{F}_{\mathrm{C,nor}}^{(i,j)} &= k_{\mathrm{n}} h^{(i,j)} \boldsymbol{n}_{ij} + \gamma_{\mathrm{n}} \boldsymbol{U}_{\mathrm{n}}^{(i,j)}, \\
\boldsymbol{F}_{\mathrm{C,tan}}^{(i,j)} &= k_{\mathrm{t}} \boldsymbol{\xi}^{(i,j)}, \\
\boldsymbol{T}_{\mathrm{C}}^{(i,j)} &= a_i \boldsymbol{n}_{ij} \times \boldsymbol{F}_{\mathrm{C,tan}}^{(i,j)},
\end{aligned} \tag{5}$$

and fulfill Coulomb's friction law $\left|\boldsymbol{F}_{\mathrm{C,tan}}^{(i,j)}\right| \leq \mu \left|\boldsymbol{F}_{\mathrm{C,nor}}^{(i,j)}\right|$. In the above expressions, k_{n} and k_{t} are the normal and tangential spring constants, respectively, and γ_{n} is the damping constant. The normal and tangential velocities are $\boldsymbol{U}_{\mathrm{n}}^{(i,j)} \equiv \boldsymbol{n}_{ij}\boldsymbol{n}_{ij} \cdot (\boldsymbol{U}^{(j)} - \boldsymbol{U}^{(i)})$ and $\boldsymbol{U}_{\mathrm{t}}^{(i,j)} \equiv (\boldsymbol{I} - \boldsymbol{n}_{ij}\boldsymbol{n}_{ij}) \cdot [\boldsymbol{U}^{(j)} - \boldsymbol{U}^{(i)} - (a_i \boldsymbol{\Omega}^{(i)} + a_j \boldsymbol{\Omega}^{(j)}) \times \boldsymbol{n}_{ij}]$. Finally, the quantity $\boldsymbol{\xi}^{(i,j)}$ is the tangential spring stretch. This contact model could be made more general, but at the price of numerical difficulties; see Appendix B.

The computation of the tangential spring stretch $\boldsymbol{\xi}^{(i,j)}$, described in the following, requires some care, as we have to impose Coulomb's law. At the time t_0 at which the contact (i,j) is created, we set an unstretched tangential spring $\boldsymbol{\xi}^{(i,j)}(t_0) = \boldsymbol{0}$. At any further time step t in the simulation, the tangential stretch $\boldsymbol{\xi}^{(i,j)}(t)$ is incremented according to the value of a "test" force $\boldsymbol{F}_{\mathrm{C,tan}}^{\prime(i,j)}(t + \mathrm{d}t) = k_{\mathrm{t}} \boldsymbol{\xi}^{\prime(i,j)}(t + \mathrm{d}t)$ with $\boldsymbol{\xi}^{\prime(i,j)}(t + \mathrm{d}t) = \boldsymbol{\xi}^{(i,j)}(t) + \boldsymbol{U}_{\mathrm{t}}^{(i,j)}(t)\mathrm{d}t$. If $\left|\boldsymbol{F}_{\mathrm{C,tan}}^{\prime(i,j)}(t + \mathrm{d}t)\right| \leq \mu \left|\boldsymbol{F}_{\mathrm{C,nor}}^{(i,j)}(t + \mathrm{d}t)\right|$, the contact is in a static friction state and we update the spring stretch and force as

$$\begin{aligned}
\boldsymbol{\xi}^{(i,j)}(t + \mathrm{d}t) &= \boldsymbol{\xi}^{\prime(i,j)}(t + \mathrm{d}t), \\
\boldsymbol{F}_{\mathrm{C,tan}}^{(i,j)}(t + \mathrm{d}t) &= \boldsymbol{F}_{\mathrm{C,tan}}^{\prime(i,j)}(t + \mathrm{d}t).
\end{aligned} \tag{6}$$

However, if $\left|\boldsymbol{F}_{\mathrm{C,tan}}^{\prime(i,j)}(t+\mathrm{d}t)\right| > \mu \left|\boldsymbol{F}_{\mathrm{C,nor}}^{(i,j)}(t+\mathrm{d}t)\right|$, the contact is in a sliding state and the spring and force are updated as

$$\begin{aligned}
\boldsymbol{\xi}^{(i,j)}(t + \mathrm{d}t) &= \frac{\mu}{k_{\mathrm{t}}} \left|\boldsymbol{F}_{\mathrm{C,nor}}^{(i,j)}(t + \mathrm{d}t)\right| \boldsymbol{t}, \\
\boldsymbol{F}_{\mathrm{C,tan}}^{(i,j)}(t + \mathrm{d}t) &= k_{\mathrm{t}} \boldsymbol{\xi}^{(i,j)}(t + \mathrm{d}t),
\end{aligned} \tag{7}$$

where the direction $\boldsymbol{t}$ is the same as the one for the test force, i.e., $\boldsymbol{t} \equiv \boldsymbol{F}_{\mathrm{C,tan}}^{\prime(i,j)}(t+\mathrm{d}t) / \left|\boldsymbol{F}_{\mathrm{C,tan}}^{\prime(i,j)}(t+\mathrm{d}t)\right|$. In this case, Coulomb's law is not violated, as $\left|\boldsymbol{F}_{\mathrm{C,tan}}^{(i,j)}(t + \mathrm{d}t)\right| = \mu \left|\boldsymbol{F}_{\mathrm{C,nor}}^{(i,j)}(t + \mathrm{d}t)\right|$.

B. Other interactions, full models

1. *Shear rate dependence: why Stokes hydrodynamics plus hard spheres is not enough*

The shear-rate dependence of a suspension requires the existence of a time scale distinct from the inverse shear rate. A well-known case is the one of Brownian suspensions, where the inverse shear rate competes with the Brownian diffusion time to give a shear-rate dependent rheology. This competition is adequately measured by a non-dimensionalized shear rate, the Péclet number, which is the ratio of the two time scales: $Pe \equiv 6\pi\eta_0 a^3 \dot{\gamma} / k_{\mathrm{B}} T$. This quantity can also be thought as a ratio of two force scales, the typical hydrodynamic force and the typical Brownian force. Thus, a shear-rate dependent rheology generically requires at least one other force scale besides the hydrodynamic one.

Such a time scale does not exist for non-Brownian suspensions of hard spheres in the Stokes regime. The reason is straightforward: the hard sphere force has no typical value, and a hard-sphere contact between two particles can withstand any applied load. Therefore there is nothing with which to compare the hydrodynamic force. This means that the solutions of the force/torque balance equations eq. (3) (i.e., the particle trajectories) are independent of the shear rate, leading to a shear-rate independent rheology. Notice that this conclusion holds whether the hard spheres are frictionless or frictional: Coulomb's law does not introduce a force scale. There must be another force scale in the system to provide the shear-rate dependence.

An important point in our model is that, even if we try to mimic a hard sphere suspension, our contact forces actually are elastic forces, thus bringing a natural force scale $k_{\mathrm{n}}a$. We preserve the shear-rate independent hard sphere behavior by selecting the particle stiffness k_{n} such that the non-dimensionalized shear rate $6\pi\eta_0 a\dot{\gamma}/k_{\mathrm{n}}$ remains much smaller than unity; i.e., we stay in the asymptotic regime of nearly hard particles. We detail the techniques we use to achieve this in our simulation in appendix B.

2. A minimal model: critical-load friction

The first model we consider is an intentionally simplistic one, arguably the simplest model with an additional force scale besides the hydrodynamic force. Simplicity is the main motivation for this model, as it enables the clear physical discussion one can expect from a minimal model.

In this model (which we call Critical Load Model, CLM), we introduce an extra force scale in the friction law itself, namely a threshold normal load F_{CL} to activate friction. When the normal load is smaller than this threshold, particles interact as frictionless hard spheres. When the load is beyond the threshold, friction is activated. Overall, the friction law reads:

$$\left|\boldsymbol{F}^{(i,j)}_{\mathrm{C,tan}}\right| \leq \begin{cases} \mu\Big(\left|\boldsymbol{F}^{(i,j)}_{\mathrm{C,nor}}\right| - F_{\mathrm{CL}}\Big) & \text{for } \left|\boldsymbol{F}^{(i,j)}_{\mathrm{C,nor}}\right| \geq F_{\mathrm{CL}}, \\ 0 & \text{otherwise.} \end{cases} \tag{8}$$

We may consider the CLM as the short Debye length limit of the electrostatic repulsion model presented below (section II B 3).

3. Electrostatic repulsion model

An electrostatic repulsion is a simple and plausible interaction. Many experimental systems have such a force, as it stabilizes the suspension. Thus, we will consider an Electrostatic Repulsion Model (ERM) including this ingredient in the simplest form of a repulsive double-layer electrostatic force $\boldsymbol{F}^{(i,j)}_{\mathrm{R}}$ [Israelachvili 2011]. If the Debye length $1/\kappa$ is small compared to the radius of the particles, the approximate form

$$\boldsymbol{F}^{(i,j)}_{\mathrm{R}}(h) \simeq \begin{cases} -2F_{\mathrm{ER}}a_i a_j/(a_i+a_j)e^{-\kappa h^{(i,j)}}\boldsymbol{n}^{(i,j)} & \text{if } h^{(i,j)} \geq 0, \\ -2F_{\mathrm{ER}}a_i a_j/(a_i+a_j)\boldsymbol{n}^{(i,j)} & \text{if } h^{(i,j)} < 0, \end{cases} \tag{9}$$

can be used. In the simulations, we set $1/\kappa = 0.05a$.

C. Stress tensor and bulk rheology

The mechanical stress applied to the suspension arises from the several interactions included in the model: particles disturb the flow, creating hydrodynamic stresses, and they develop force chains via contacts (and/or electrostatic repulsion for the ERM).

The hydrodynamic stresslets acting on the particles are given by [Brady and Bossis 1988, Batchelor 1970]

$$\boldsymbol{S}_{\mathrm{H}} = -\left(\boldsymbol{R}^{S}_{\mathrm{Stokes}} + \boldsymbol{R}^{S}_{\mathrm{Lub}}\right) \cdot \begin{pmatrix} \boldsymbol{U} - \boldsymbol{U}^{\infty} \\ \boldsymbol{\Omega} - \boldsymbol{\Omega}^{\infty} \end{pmatrix} + \boldsymbol{R}'^{S}_{\mathrm{Lub}} : \boldsymbol{E}^{\infty}, \tag{10}$$

where $\boldsymbol{S}_{\mathrm{H}} \equiv \left(\boldsymbol{S}^{(1)}_{\mathrm{H}}, \ldots, \boldsymbol{S}^{(n)}_{\mathrm{H}}\right)$ and the matrices $\boldsymbol{R}^{S}_{\mathrm{Lub}}$ and $\boldsymbol{R}'^{S}_{\mathrm{Lub}}$ contain leading terms of the lubrication resistances [Jeffrey and Onishi 1984, Jeffrey 1992] (see appendix A) in a manner consistent with the hydrodynamic forces considered in II A 2.

The stress due to the contact or repulsive force between particles i and j is simply written as

$$\boldsymbol{S}^{(i,j)}_{\mathrm{C}} = (\boldsymbol{r}^{(j)} - \boldsymbol{r}^{(i)})\boldsymbol{F}^{(i,j)}_{\mathrm{C}} \text{ or } \boldsymbol{S}^{(i,j)}_{\mathrm{R}} = (\boldsymbol{r}^{(j)} - \boldsymbol{r}^{(i)})\boldsymbol{F}^{(i,j)}_{\mathrm{R}}, \tag{11}$$

respectively.

The bulk stress, in which the isotropic part of the fluid pressure is omitted, is the sum of the above contributions:

$$\boldsymbol{\Sigma} \equiv 2\eta_0 \boldsymbol{E}^{\infty} + \frac{1}{V}\left(\sum_i \boldsymbol{S}^{(i)}_{\mathrm{H}} + \sum_{i>j} \boldsymbol{S}^{(i,j)}_{\mathrm{C}} + \sum_{i>j} \boldsymbol{S}^{(i,j)}_{\mathrm{R}}\right), \tag{12}$$

where V is the volume of the simulation box (the electrostatic stress $\boldsymbol{S}_{\mathrm{R}}$ appears only for the ERM). Shear stress σ, normal stress differences N_1 and N_2, and particle pressure Π [Yurkovetsky and Morris 2008] are defined as $\sigma \equiv \Sigma_{12}$, $N_1 \equiv \Sigma_{11} - \Sigma_{22}$, $N_2 \equiv \Sigma_{22} - \Sigma_{33}$, and $\Pi \equiv -(\Sigma_{11} + \Sigma_{22} + \Sigma_{33})/3$, respectively. The relative viscosity η_{r} is given by $\eta_{\mathrm{r}} \equiv \sigma/\eta_0\dot{\gamma}$.

D. Additional points in the simulation model

a. Bidispersity: We consider a suspension of bidisperse frictional hard spheres immersed in a Newtonian fluid with viscosity η_0. The bidispersity is introduced to hinder the formation of the ordered phase observed for dense monodisperse suspensions under shear. An effective choice for the size ratio is $a_2/a_1 = 1.4$ (where $a_1 = a$), with the two populations occupying equal volumes; i.e., $\phi_1 = \phi_2$.

b. Dimensionless shear rate: We discussed in II B 1 that another force scale besides the hydrodynamic one is required to yield shear-rate dependence. In CLM, the threshold value gives the force scale $F^* = F_{\mathrm{CL}}$, and in ERM, the force at contact gives $F^* = F_{\mathrm{ER}}$. Therefore, the shear rate dependence is essentially given by the ratio $\dot{\gamma}/\dot{\gamma}_0$, with $\dot{\gamma}_0 \equiv F^*/6\pi\eta_0 a^2$.

c. Periodic boundary conditions and fixed-volume simulation: Rheology is a bulk property. If solid walls are used for the boundaries of the system, we need a large system size to reduce the influence of walls. We can avoid the use of solid walls in a simulation by using periodic boundary conditions. For the strain-controlled simple shear, we can use the Lees-Edwards [Lees and Edwards 1972] boundary condition.

Particle migration never develops under these periodic boundary conditions. Although some experimental observations suggest that global migration may be a cause of shear thickening [Fall *et al.* 2010], our simulation is free of this effect.

There is no way for the system to dilate with these periodic boundary conditions. Such a fixed volume condition is expected in most rheology measurements. For shear thickening fluids, however, the open edges may have some influence [Brown and Jaeger 2012]. In granular physics, systems are sheared under a given normal stress, hence the volume is not fixed [Boyer *et al.* 2011].

III. RESULTS

This section presents the results from the simulation of the two models, the "minimal" critical load model (CLM) and the electrostatic repulsion model (ERM). In the following subsections, whenever possible, the two models are treated at the same time in the text, and we will show data plots for the CLM. However, when the two models give slightly different results, the results of the CLM will be described first, as it allows a simple and clear understanding of the underlying physics, and the more realistic model ERM will be described afterwards. The differences are essentially in the low shear rate limit (existence of a shear-thinning regime) for the ERM, due to the repulsive potential.

The data shown here are obtained for a friction coefficient $\mu = 1$ except for the part showing the dependence on μ.

A. Frictionless and frictional rheologies

In the CLM, due to the threshold force, the friction between grains is absent at low shear rates, and activated at high shear rates. Because of this, we expect that the low shear-rate limit for concentrated suspensions will have a rheology $\eta(\phi, \dot{\gamma} \to 0)$ typical of a system close to the jamming transition for frictionless particles, while the high shear-rate limit shows a rheology $\eta(\phi, \dot{\gamma} \to \infty)$ typical of a system close to the jamming transition for particles with a friction coefficient $\mu = 1$.

These two limiting viscosities are shown in FIG. 1, where we also show the high shear-rate behavior for the infinite friction case ($\mu = \infty$), for reference. Each diverges at a different volume fraction, thus friction shifts the jamming point [Otsuki and Hayakawa 2011]. We fit our data with power law divergences $\eta \propto C(1 - \phi/\phi_J)^{-\lambda}$, with parameters (ϕ_J, λ, C) as detailed in the caption of FIG. 1.

For the ERM, the situation is the same at high shear rates, but differs at low shear rates. While friction is not felt for $\dot{\gamma} \to 0$, as particles do not contact, the finite range of the repulsive potential creates a shear thinning behavior from which we could not obtain the low shear-rate limit $\eta(\phi, \dot{\gamma} \to 0)$. This comes from the fact that at $\dot{\gamma} = 0$, the system behaves essentially as soft particles with an apparent size that includes the hard sphere and the surrounding soft repulsive potential. The jamming transition of these bigger soft frictionless particles is at an apparent packing fraction (based on the apparent diameter) $\phi' = \phi_J'^{\mu=0}$, which corresponds to an actual packing fraction ϕ significantly lower than $\phi_J'^{\mu=0}$. Because of this low volume fraction jamming transition at $\dot{\gamma} = 0$, the viscosity is larger than at small $\dot{\gamma}$, leading to the shear thinning we observe.

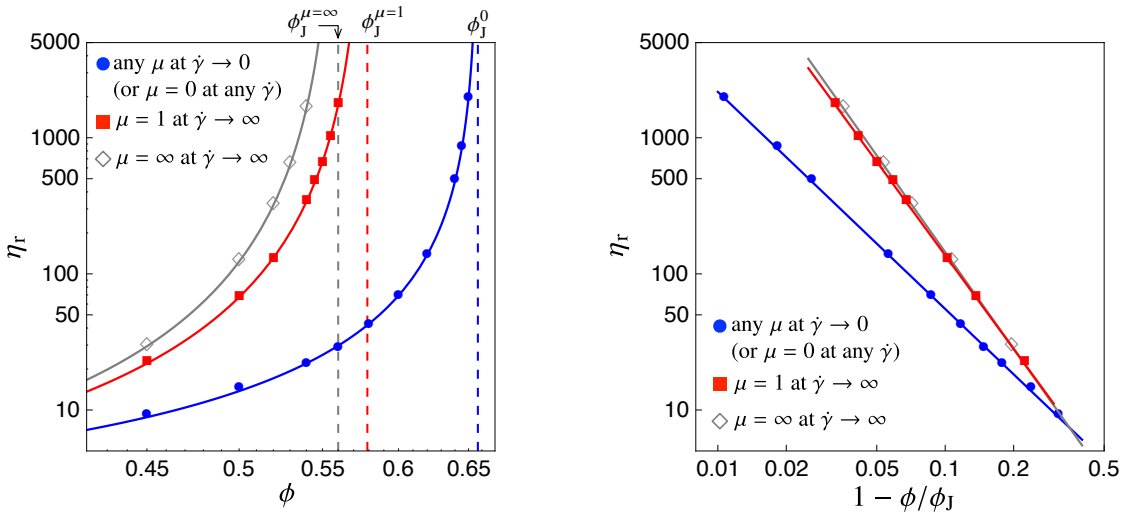

FIG. 1. Relative viscosity η_r as a function of the volume fraction ϕ in the two limits $\dot\gamma \to 0$ and $\dot\gamma \to \infty$ (left). The $\dot\gamma \to 0$ viscosity (blue circles) is independent of the friction coefficient μ as the friction is not activated at low stresses, which leads to a relatively lower viscosity diverging at a higher volume fraction ϕ_J^0 (which is the jamming point for frictionless systems). The $\dot\gamma \to \infty$ viscosity however directly depends on μ, as is seen from the difference between $\mu = 1$ (red squares) and $\mu = \infty$ (gray diamonds) plots. In particular, the jamming volume fraction decreases with increasing μ. We fit our data with power laws $\eta_r = C(1 - \phi/\phi_J)^{-\lambda}$ (right). The best fitting parameters are $(\phi_J^0, \lambda^0, C^0) \approx (0.66, 1.6, 1.40)$, $(\phi_J^{\mu=1}, \lambda^{\mu=1}, C^{\mu=1}) \approx (0.58, 2.3, 0.71)$, and $(\phi_J^{\mu=\infty}, \lambda^{\mu=\infty}, C^{\mu=\infty}) \approx (0.56, 2.4, 0.63)$.

B. Shear thickening, continuous and discontinuous

We can switch from one rheology to the other by varying the shear rate. Physically, the transmitted stress increases as the shear rate increases, which triggers the formation of frictional contacts between particles. Thus, by increasing the shear rate, the viscosity interpolates between the frictionless and frictional rheology curves, which means we can observe shear thickening. All this should be a natural consequence of the existence of two distinct rheologies at $\dot\gamma = 0$ and $\dot\gamma = \infty$. What we cannot anticipate *a priori* is the way in which the system switches from the low viscosity state to the high viscosity one: do we observe a Continuous Shear Thickening (CST) or a Discontinuous Shear Thickening (DST)?

The shear rate dependence of the viscosity, shown in FIG. 2 for the CLM, demonstrates the existence of both CST and DST in our system, depending on the volume fraction. As in experiments, when $\phi < \phi_c$ the shear thickening is continuous, getting steeper and steeper as we approach ϕ_c, at which point it becomes discontinuous and keeps this behavior for $\phi > \phi_c$ and up to ϕ_J^0. Note that there appears to be a real discontinuity in our data for these volume fractions: the time series of the viscosity show an intermittent behavior switching between two states, that we detail in the next section. In FIG. 2, the intermittent data are split (two points appear at the same shear rate) and represent a time average for each of the two states.

When plotted against stress in FIG. 2, the viscosity curves show another interesting feature, namely that the onset of shear thickening occurs at a stress that is roughly independent of the volume fraction. From a mild shear thickening to a marked DST, this stress

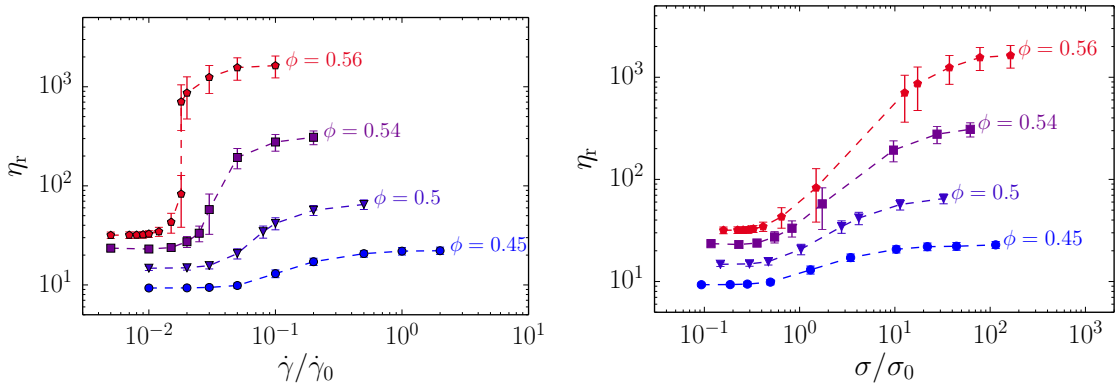

FIG. 2. Shear rate $\dot\gamma$ (left) and shear stress σ (right) dependences of the relative viscosity η_r for the critical load model (CLM), with friction coefficient $\mu = 1$, for volume fractions $0.45 \leq \phi \leq 0.56$. The system size is $N = 1000$. The error bars represent the standard deviation.

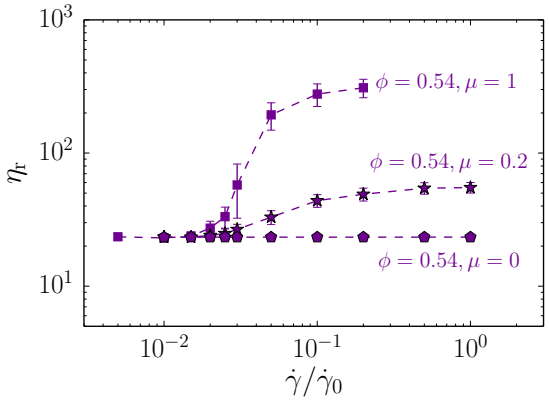

FIG. 3. Effect of the friction coefficient μ on the shear rate dependence of the relative viscosity $\eta_r(\dot\gamma)$ in the CLM. The friction is essential to the shear thickening, as is illustrated by the reduction of the effect for $\mu = 0.2$ and its complete suppression for $\mu = 0$.

remains constant, as expected from a simple balance argument between the driving stress $\sigma = \eta\dot\gamma$ and the stress required to create a frictional contact $\sim F_{\rm CL}/a^2$ (for the CLM) which implies the transition should take place for $\sigma_{\rm ST} \simeq F_{\rm CL}/a^2$. Indeed, we numerically find $\sigma_{\rm ST} = 6\pi\sigma/\sigma_0 \approx 6$, which is compatible with our estimate of $\sigma_{\rm ST} \simeq F_{\rm CL}/a^2 = 1$.

Friction is an essential ingredient for the shear thickening to occur, as is illustrated in FIG. 3, which shows the effect of a reduction of the friction coefficient on the $\eta_r(\dot\gamma)$ curve in the CST regime. If the friction is removed ($\mu = 0$), the effect is completely suppressed (this is expected, as the threshold force scale $F_{\rm CL}$ disappears from the equations of motion for $\mu = 0$, and the simulation is then rigorously the same for all $\dot\gamma$). If the friction is only reduced ($\mu = 0.2$), the shear thickening is milder than with $\mu = 1$ friction at the same volume fraction. In that case, the CST however becomes more pronounced and turns to DST when one increases the volume fraction, just as for the $\mu = 1$ case.

The ERM shown in FIG. 4 behaves in a very similar manner, only adding a shear thinning regime at low shear rates.

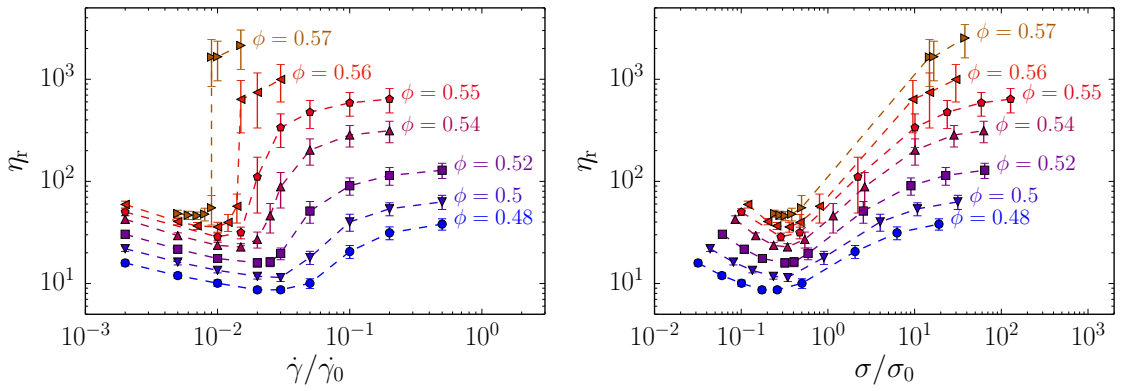

FIG. 4. Shear rate $\dot{\gamma}$ (left) and shear stress σ (right) dependences of the relative viscosity η_r for the electrostatic repulsion model (ERM), with Debye length $1/\kappa = 0.05a$ and friction coefficient $\mu = 1$, for volume fractions $0.48 \leq \phi \leq 0.57$. The system size is $N = 512$. The error bars represent the standard deviations.

C. Discontinuity and hysteresis

The existence of two distinct flowing states suggests that one might expect to observe a hysteresis associated with DST. It is thus remarkable that, aside from suspensions that are hysteretic at the microscopic level (with attractive interactions, for example, since once particles are aggregated under flow they stay aggregated upon cessation of the flow), there are very few experimental reports of hysteresis in systems showing DST (one of the best examples is provided by Bender and Wagner [1996]).

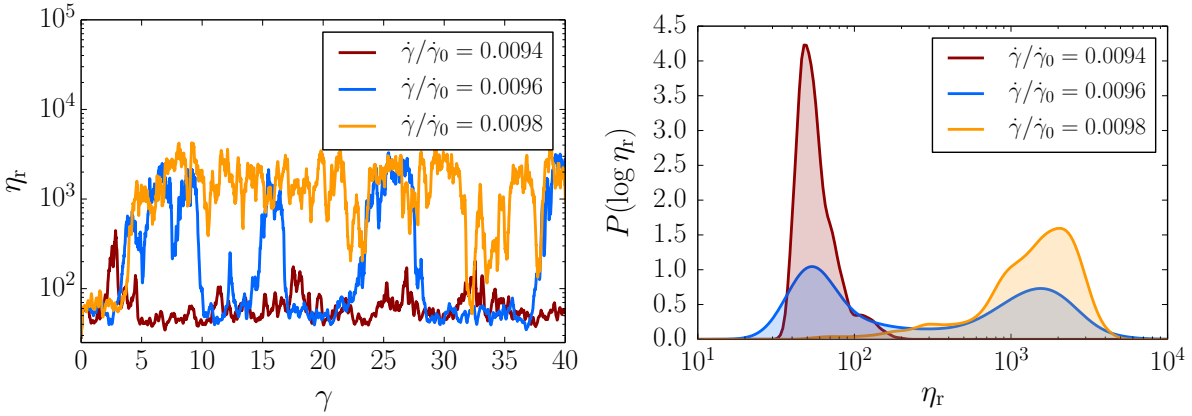

FIG. 5. Strain (or dimensionless time) series of the shear stress close to the DST (left), and the corresponding histograms (right). The simulations are performed at $\phi = 0.57$ with the ERM, with shear rates $\dot{\gamma}/\dot{\gamma}_0 = 0.0094$ (just below the DST region), $\dot{\gamma}/\dot{\gamma}_0 = 0.0096$ (in the DST region), and $\dot{\gamma}/\dot{\gamma}_0 = 0.0098$ (just above the DST region). Data at $\dot{\gamma}/\dot{\gamma}_0 = 0.0096$ show a superposition of the two states. This is very similar to what is seen in experiments [Boersma *et al.* 1991].

What is commonly observed, however, is a switching behavior, where the time series of the stress shows that the system shares its time between the two states, erratically switching in what looks like activated events [D'Haene *et al.* 1993, Bender and Wagner 1996, Lootens

et al. 2004, 2005, 2003, Hébraud and Lootens 2005, Boersma *et al.* 1991]. We observe this switching behavior in both models that we studied. In FIG. 5 we show time series of the stress and the corresponding histograms around the DST. These data show a typical "coexistence" behavior: significantly below and above shear thickening, the system respectively stays in the low and high viscosity state. But close to DST, the two states coexist in the same time series, the exact blend being determined by the shear rate. The proportion of time spent in the high viscosity state increases with $\dot{\gamma}$. A switching behavior is obtained in a small range of shear rates around $\dot{\gamma}/\dot{\gamma}_0 = 0.0096$ for $\phi = 0.57$, and one expects this range to broaden as we increase the volume fraction, as is predicted by an S-shaped flow curve [Wyart and Cates 2014].

In order to observe a hysteresis in the system, one must have a system where the relaxation time τ_{relax} (the length of the transient) is much smaller than the activation time τ_{act} (the typical time between two switches). One then does a proper measurement with a shear rate sweep on a time scale τ_{sw} such that $\tau_{\text{relax}} \ll \tau_{\text{sw}} \ll \tau_{\text{act}}$: the first inequality ensures that the system is always in a steady state during the sweep and that the measurement is done with sufficient time averaging, while the second inequality ensures that we are not averaging data over two distinct states. In our simulations, as can be seen by looking at the time series in FIG. 5, a clear separation of time scales is not achieved (we have $\tau_{\text{relax}} \lesssim \tau_{\text{act}}$, which does not permit finding a proper τ_{sw}) and hysteresis cannot be observed unambiguously. Many experimental data actually suffer from the same limitations, and this might be the reason for the very small number of hysteretic flow curves actually reported. One exception is the noted work of Bender and Wagner [1996].

D. Normal stresses

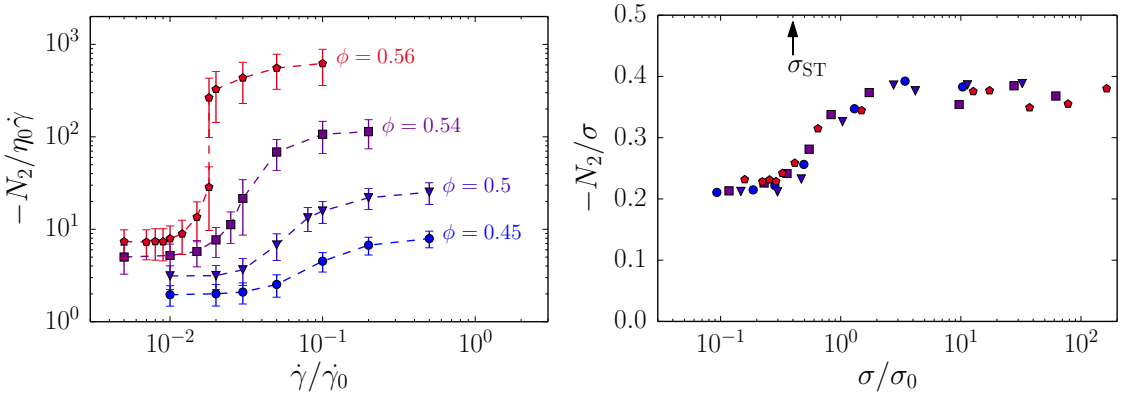

FIG. 6. Shear rate dependence of the normalized second normal stress difference $N_2/\eta_0\dot{\gamma}$ (left) and shear stress dependence of N_2/σ (right) for the CLM. The stress σ_{ST} at which thickening starts is marked by an arrow.

One common rheological characteristic of dense suspensions is the appearance of normal stress differences. Our measurements of the two normal stress differences N_1 and N_2 are shown in FIG. 6 and 7 for the CLM. The ERM behaves very similarly and is not shown.

We obtain for N_2 a behavior consistent with most experimental data available: it is negative, large, and its behavior is reminiscent of that of the shear stress. This comes from

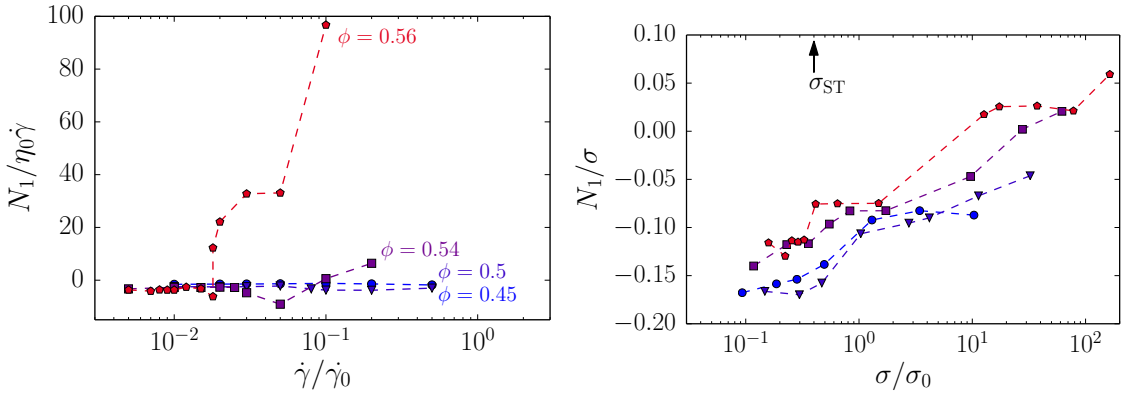

FIG. 7. Shear rate dependence of the normalized first normal stress difference $N_1/\eta_0\dot{\gamma}$ (left) and shear stress dependence of N_1/σ (right) for the CLM.

the fact that most of the stress is transmitted by forces in the shear plane (flow-gradient), not along the vorticity direction. Indeed the ratio N_2/σ is insensitive to the stress magnitude, increasing at most by a factor of two across shear thickening while the stresses increase by almost two orders of magnitude. What is remarkable is the independence of N_2/σ on the volume fraction: all volume fractions investigated here collapse on a master curve for both models.

There has been debate in the community regarding the value (and even the algebraic sign) of N_1. The first noticeable feature of our data concerning N_1 is that it is dominated by the fluctuations, not the average. In one time series, a cursory look indicates that its value fluctuates around zero. Long time averaging reveals more structure, however, as shown in FIG. 7 for the CLM. Prior to shear thickening, the average of N_1 is nearly zero (slightly negative for CLM, slightly positive for ERM). The shear thickening transition is marked by two different behaviors, depending on the volume fraction: at the lowest volume fractions studied, N_1 decreases across shear thickening, while at larger ϕ there is a clear upturn towards positive values at the shear thickening transition. For the CLM, the behavior can be systematized by plotting N_1 as a function of the stress, as in FIG. 7: N_1/σ is an increasing function of σ, with a qualitative behavior roughly independent of ϕ. The same plot for the ERM is similar but less systematic. In any case, even above shear thickening, the ratio N_1/σ is always small, not exceeding 0.1.

Overall, the behavior we observe for N_1 is consistent with some experiments [Lootens *et al.* 2005, Larsen *et al.* 2010, Lee *et al.* 2006, Couturier *et al.* 2011, Dbouk *et al.* 2013] (although [Lee *et al.* 2006] also observe a subsequent change towards negative N_1 at very high shear rates, and [Dbouk *et al.* 2013] find a positive but significantly larger N_1), but not all ([Zarraga *et al.* 2000, Singh and Nott 2003, Dai *et al.* 2013] report a negative N_1). In any case the amplitude of the fluctuations seems to be the relevant physical information about N_1, as the average, positive or negative, is buried in the fluctuations in the time series, such that at any time N_1 can be either positive or negative, even at large ϕ and $\dot{\gamma}$.

E. Microstructure

The question of the evolution of the microstructure across shear thickening is essential. Ideas associated with the order-disorder transition scenario [Hoffman 1972, 1974, 1998] predicted a clear structural change with shear thickening. Experimental observations, however, revealed that the low viscosity state was not always ordered and that the shear thickening can occur with only a subtle signature in the microstructure [Bender and Wagner 1996, Maranzano and Wagner 2002, Watanabe *et al.* 1997, 1998, Newstein *et al.* 1999]. One suggestion comes from the hydroclustering scenario, which assumes the existence of hydrodynamically created extended density fluctuations. Some experimental data are indeed in qualitative agreement with this scenario [Maranzano and Wagner 2002, Cheng *et al.* 2011].

In the scenario we suggest in this article, the main structural modifications across the shear thickening transition should be sought in the contacts between particles. At low shear rates, frictional contacts are avoided because the particle pressure is too small to overcome the threshold (for the CLM) or the repulsion between particles (for the ERM). Those changes should thus be detected by measures specifically sensitive to the contacts. The pair correlation function should show few dramatic modifications across shear thickening. This is what we show in this section.

We define the pair correlation function:

$$g_{\mathrm{all}}(\boldsymbol{r}) \equiv \frac{V}{N^2} \sum_{i,j} \delta(\boldsymbol{r} - \boldsymbol{r}_{ij}). \tag{13}$$

The system being bidisperse, we can also define partial pair correlation functions restricted to, e.g., pairs of small-small particles $g_{\mathrm{SS}}(\boldsymbol{r}) \equiv (V/N_{\mathrm{S}}^2) \sum_{i,j \in \mathcal{S}_{\mathrm{S}}} \delta(\boldsymbol{r} - \boldsymbol{r}_{ij})$ where $\mathcal{S}_{\mathrm{S}}$ is the subset of N_{S} small particles. In the same way, we define the structure factor (which is related to the pair correlation function via a Fourier Transform) as

$$S_{\mathrm{all}}(\boldsymbol{k}) \equiv \frac{1}{N} \sum_{i,j \in \mathcal{S}, i \neq j} e^{i\boldsymbol{k}.\boldsymbol{r}_{ij}}. \tag{14}$$

In FIG. 8 and 9, we show the pair correlation function restricted to the shear plane (velocity/gradient) at $\phi = 0.57$ for four values of the shear rate: $\dot{\gamma}/\dot{\gamma}_0 = 0.005$, well below DST; $\dot{\gamma}/\dot{\gamma}_0 = 0.0094$, just below DST; $\dot{\gamma}/\dot{\gamma}_0 = 0.0098$, just above DST and $\dot{\gamma}/\dot{\gamma}_0 = 0.015$, well above DST. As expected, the evolution of those plots seems weak around DST. The main feature is a loss of contrast, unveiling a more isotropic structure above shear thickening.

The structure factor FIG. 10 reveals another interesting feature: there is a clear anisotropy in the shear plane in the low viscosity state, with a peak in the gradient direction that is strongly reduced (but not absent, see the right of FIG. 10) in the high viscosity state, above DST. This anisotropy is absent in the flow-vorticity plane; see FIG. 11. Looking back at the pair correlation functions in FIG. 8, we see that the peak of $S_{\mathrm{all}}(\boldsymbol{k})$ along the gradient direction is the signature of a slight ordering of the low viscosity phase: there are small but visible downstream ripples aligned with the flow direction at small shear rate.

The slight layering we observe is however quite far from the string order usually associated with the order-disorder scenario. In the Supplementary Material, we show movies of the system projected on the gradient-vorticity plane (i.e., looking down the stream direction), for shear rates just below and just above shear thickening, where we reduced the size of the particles to a third of their actual radius to allow a better visualization. Those movies

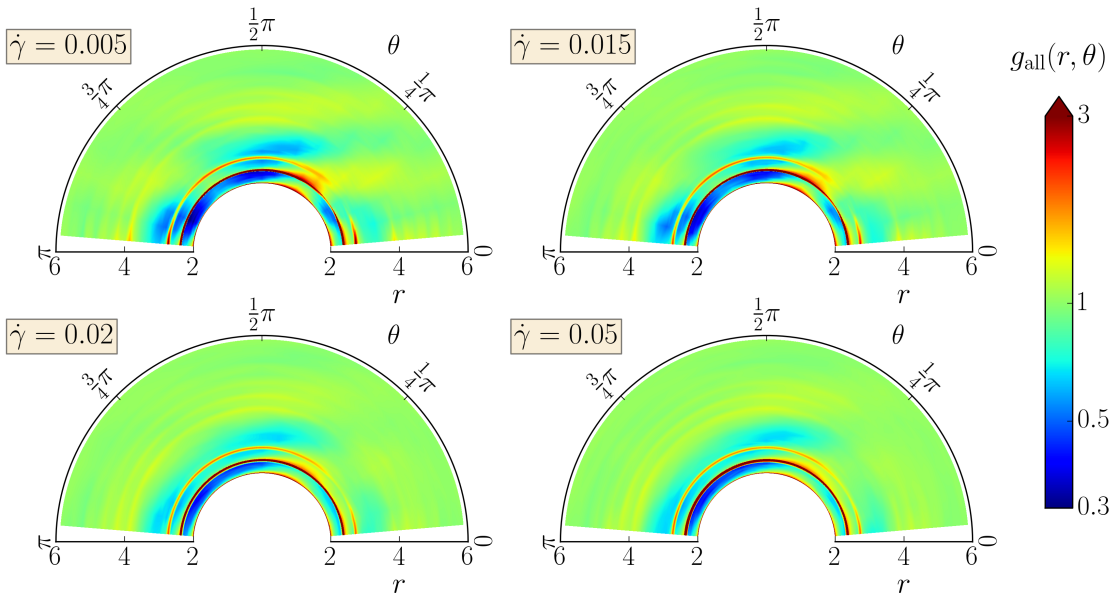

FIG. 8. Pair correlation functions restricted in the shear plane $g_{\rm all}(r,\theta)$ for the CLM at $\phi = 0.56$. The four plots correspond to shear rates $\dot\gamma = 0.005$ (well below DST), $\dot\gamma = 0.015$ (just below DST), $\dot\gamma = 0.02$ (just above DST), and $\dot\gamma = 0.05$ (well above DST).

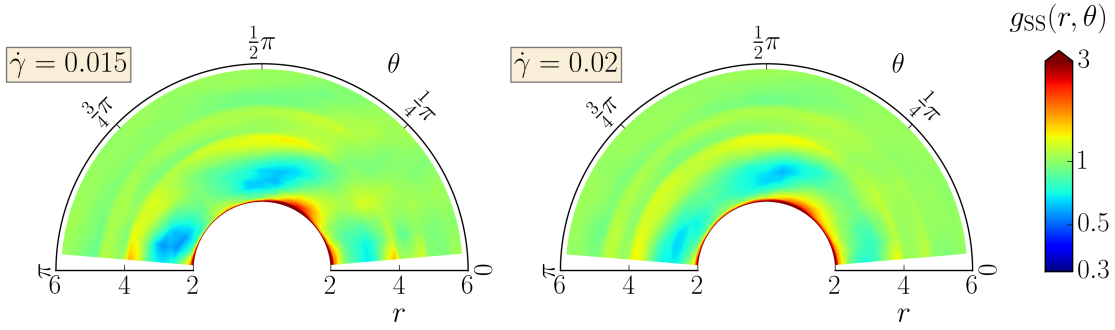

FIG. 9. Pair correlation functions restricted to pairs of small particles in the shear plane $g_{\rm SS}(r,\theta)$ for the CLM at $\phi = 0.56$. The two plots correspond to shear rates $\dot\gamma = 0.015$ (just below DST) and $\dot\gamma = 0.02$ (just above DST).

show warped layers along the flow-vorticity plane in some parts of the system, while in other parts ordered layers are completely absent. In any case, there is no further string ordering within the layers. This is consistent with our structure factor data in the gradient-vorticity direction (not shown), which shows only some structure in the gradient direction, and no six-fold symmetry patterns typically observed when string ordering takes place [Laun *et al.* 1992, Kulkarni and Morris 2009].

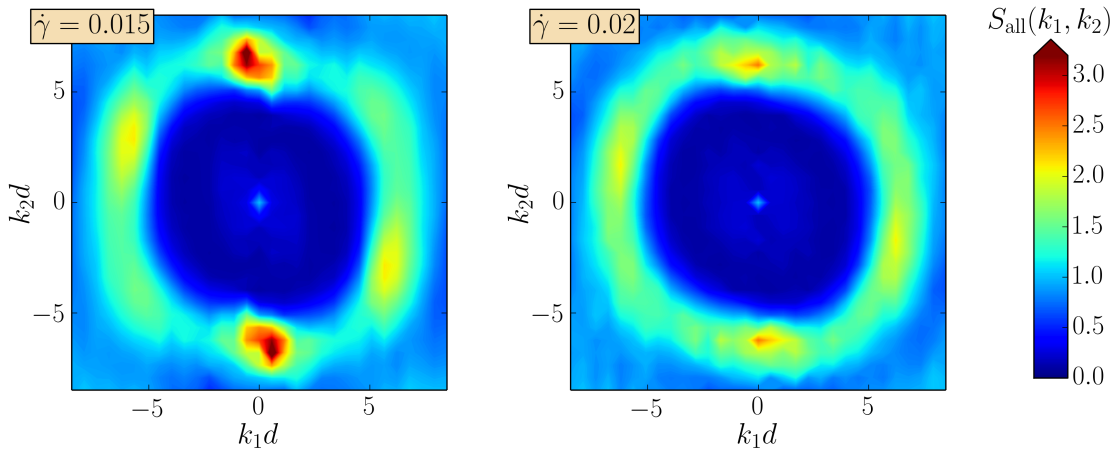

FIG. 10. Structure factor in the shear plane $S_{\mathrm{all}}(k_1, k_2)$ for the CLM at $\phi = 0.56$. Left: $\dot{\gamma} = 0.015$ (just below DST). Right: $\dot{\gamma} = 0.02$ (just above DST). The low viscosity state shows a peak in the gradient direction (around $k_1 \approx 2\pi/d$) associated with a small amount of layering, which is strongly attenuated in the high viscosity phase.

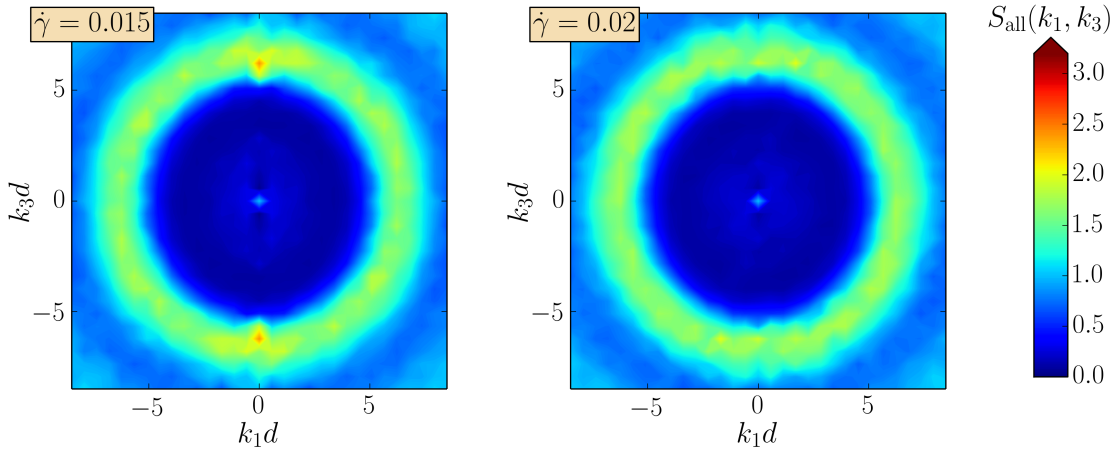

FIG. 11. Structure factor in the flow-vorticity plane $S_{\mathrm{all}}(k_1, k_3)$ for the CLM at $\phi = 0.56$. Left: $\dot{\gamma} = 0.015$ (just below DST). Right: $\dot{\gamma} = 0.02$ (just above DST). In this plane, the structure is isotropic in both states.

IV. DISCUSSION

A. Contact network

In our simulation, the shear thickening transition is due to the appearance of a growing number of frictional contacts as the shear rate (or more precisely the shear stress) increases. The contact network that is built across shear thickening is shown in FIG. 12 for the CLM for the two cases of CST and DST, respectively. (Two movies showing $\dot{\gamma}/\dot{\gamma}_0 = 0.015$ and 0.018 of DST are available in the Supplementary Material. The time in these movies is scaled with $1/\dot{\gamma}$.)

At low shear rate, in the low viscosity state, frictional contact bonds only seldomly appear,

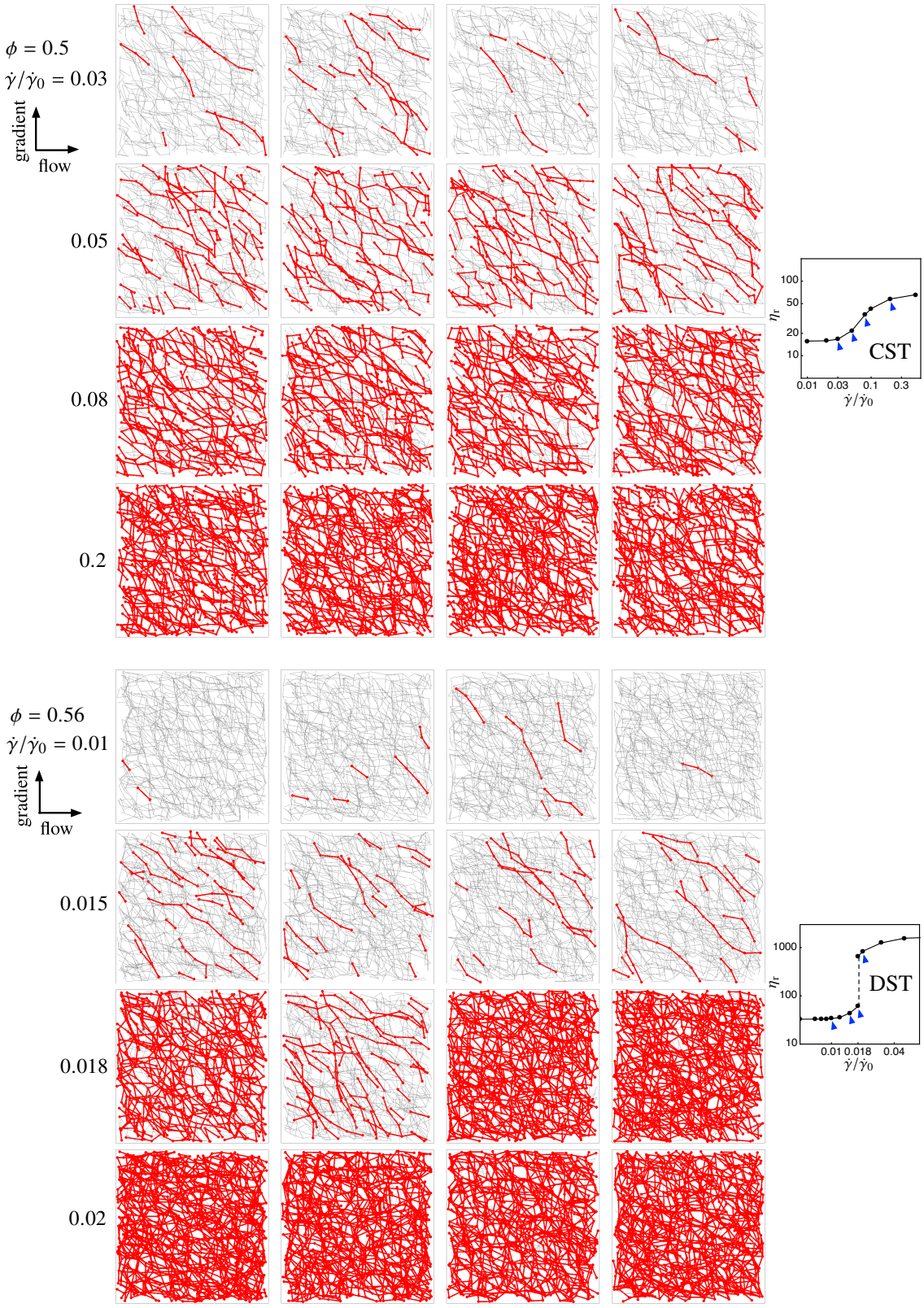

FIG. 12. Snapshots of the contact network for the CLM at $\phi = 0.5$ (upper) and 0.56 (lower). Each row corresponds to a single shear rate, ranging from the low viscosity state to the high viscosity state and across CST (upper) and DST (lower). For each shear rate, we show four snapshots at different times (or equivalently strains) along the same simulation.

being concentrated in small force chains along the compressional axis. At high shear rate, frictional contacts are the norm, creating a frictional contact network that is very close to being jammed; i.e., having only a few (collective) degrees of freedom left to reorganize under the applied stress.

Between those two extreme situations, a whole continuum of gradually denser frictional contact networks is seen across the CST transition in FIG. 12 (upper). But in the case of DST in FIG. 12 (lower), the contact network discontinuously changes from sparse to dense at the transition, never showing configurations of intermediate densities. Another interesting point is the occurrence of intermittency in the contact network, which is the immediate structural origin of the intermittent stress behavior shown in FIG. 5: close to DST, the contact network suddenly switches from mostly frictionless to mostly frictional, showing a large sensitivity to fluctuations. When this happens, the viscosity immediately follows, by switching to high/low viscosity when the contact network respectively densifies/loosens.

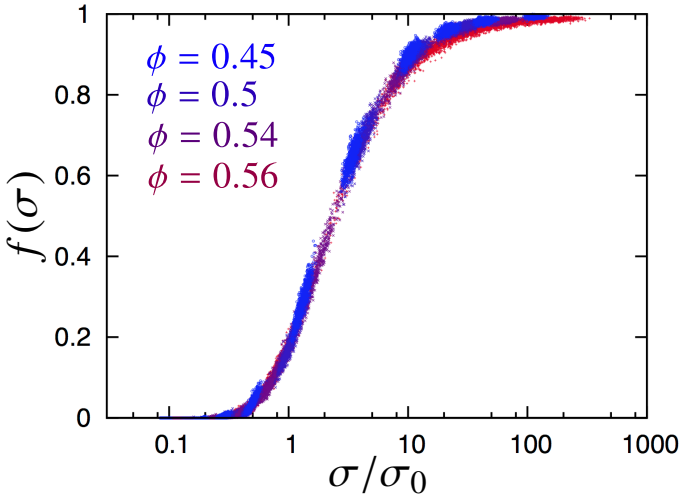

FIG. 13. The fraction of frictional contacts f as a function of the shear stress σ, for several volume fractions. There is a direct relation between the stress and the proportion of frictional contacts, which emphasizes the fundamental role of friction in shear thickening.

We can make the link between frictional contacts and shear stress explicit by looking at the fraction of frictional contacts f [Wyart and Cates 2014]. This quantity is unambiguously defined in the CLM model as the ratio of the number of contacts $N_{\mathrm{C}}^{\mathrm{f}}$ that are in the frictional state (those for which the normal force exceeds the critical load F_{CL}) divided by the total number of contacts N_{C}. This ratio has a direct relation to the shear stress, as the function $f(\sigma)$ plotted in FIG. 13 shows. This single relation demonstrates that, more than structural aspects, the shear thickening is above all a manifestation of the proliferation of frictional contacts in the system. We note one remarkable aspect of the relation $f(\sigma)$: it is independent of the volume fraction, at least in the range of ϕ that we have studied (which is rather large, owing to the fact that it should be understood as a range of distance to jamming $\phi - \phi_{\mathrm{J}}^{\mu}$ rather than a bare range of ϕ). This peculiar aspect will be studied in a separate article.

B. Phase diagram, relation to jamming

While the jamming transition is the critical phenomenon underlying DST, it should be noted that the jamming transition and DST are distinct, and in particular $\phi_c \neq \phi_J^\mu$. According to a recent theoretical argument by Wyart and Cates [2014], a scenario based on two diverging rheologies like the one we present in this work implies under reasonable assumptions that $\phi_c < \phi_J^\mu$; i.e., DST could then occur between two flowable (unjammed) states for volume fractions $\phi_c < \phi < \phi_J^\mu$.

In our simulations, we estimate $\phi_J^{\mu=1} \approx 0.58$ (see FIG. 1), while we observe DST for $\phi = 0.56$ (see FIG. 2), which indeed implies $\phi_c < \phi_J^{\mu=1}$ for our simulation. For a volume fraction $\phi > \phi_J^{\mu=1}$ only the low viscosity state would be visible under shear, because the high viscosity frictional system is jammed at this volume fraction. This sets a maximum shear rate for the shear of our system at this volume fraction.

These ideas can be summed up in a phase diagram presented in FIG. 14. In the lower part of the diagram, the rheology is essentially frictionless, as the stress is too small to activate friction between grains. This rheology diverges at the frictionless jamming point ϕ_J^0. In the upper part of the diagram, the rheology is frictional, as friction is activated under the applied stress. This rheology diverges at the frictional jamming point ϕ_J^μ and thus shows a larger viscosity than the frictionless rheology. Thus two rheologies coexist on the shear rate-volume fraction plane. Those rheologies are separated by a shear thickening that is continuous for $\phi < \phi_c$ and discontinuous for $\phi_c < \phi < \phi_J^\mu$.

The discontinuity is actually related to the coexistence of the two rheologies in the triangle delimited by a dashed line. In this region, we observe one consequence of the coexistence in the intermittency of the flow: the system switches from one state to the other through activation events, as is shown by the time series of the stress (see FIG. 5). For $\phi_J^\mu < \phi < \phi_J^0$, DST is strictly speaking no longer observed, as the high viscosity flowable state does not exist any more. In this region, DST is actually replaced by shear jamming [Bi *et al.* 2011]: if one applies a shear stress larger than σ_{ST}, the system goes to a solid state and refuses to flow. This implies the existence of a forbidden region, in gray, where no flow is possible for hard spheres. In the lower shear-rate domain above ϕ_J^μ, the low viscosity state is stable, but the activated events responsible for the intermittency at lower ϕ in small systems might lead to complete jamming in a finite time. Lastly, the dot in the upper left corner of the DST region is a critical point separating CST from DST. It shares some features with a critical point of a second order phase transition, for instance a diverging susceptibility $\mathrm{d}\sigma/\mathrm{d}\dot{\gamma}$.

Of course, as we numerically work with a shear-rate controlled scheme, the system always flows at any shear rate and any volume fraction, even in the forbidden region of the phase diagram. But this is only done by creating large overlaps between the particles (i.e., compressing them), hence violating the criteria we set to mimic hard sphere suspensions. At high shear rate and for $\phi > \phi_J^\mu$, a real hard sphere system would not flow, but it does in the simulation because of our inability to enforce the hard sphere condition in a high (possibly infinite) stress state. The spheres we simulate in that case cannot be considered hard any more, and their stiffness sets a cutoff to the stress scales under shear. This situation is somehow similar to the one observed in experiments, where it is observed that the stress in the high viscosity state is set by the weakest stress scale in the sample (which might be a large stress scale for the rheometer usage range), whether it is the particles' stiffness or the surface tension on the edge of the rheometer [Brown and Jaeger 2012]. Therefore, in an experiment, even if the idealized system would be jammed under the investigated conditions,

the real system still flows, perhaps thanks to dilation, whereas in our simulation, under the same conditions, it still flows thanks to the deformability of particles.

The difference between ϕ_c and ϕ_J^μ may have been observed in some stress drop experiments [O'Brien and Mackay 2000, Larsen *et al.* 2010]. For $\phi_c < \phi < \phi_J^\mu$, the phase diagram of FIG. 14 predicts that the stress in the thickened state would relax quickly upon flow cessation, as the contact network is unjammed. By contrast, for $\phi_J^\mu < \phi < \phi_J^0$ the stress would not relax entirely, as part of it would be stored elastically in the jammed contact network. This scenario is actually consistent with the data from O'Brien and Mackay [2000], Larsen *et al.* [2010].

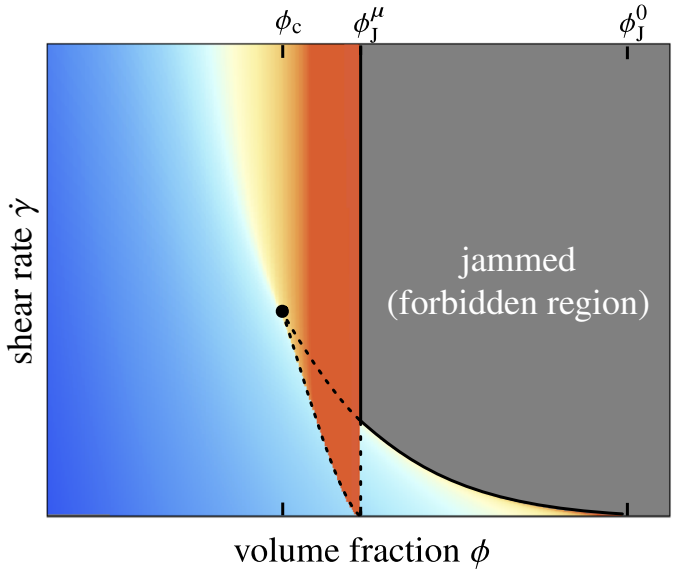

FIG. 14. Schematic phase diagram in the shear rate-volume fraction plane. The viscosity is color coded, from small (blue) to large values (red). Along the ϕ axis, ϕ_c is the point above which we can observe DST, ϕ_J^μ is the jamming point for frictional spheres with friction coefficient μ, and ϕ_J^0 is the jamming point for frictionless spheres. Intermittency is observed in the region delimited by a dashed line.

V. CONCLUSION

We have introduced a frictional-viscous model of dense suspensions under shear that is built on the framework used by previous standard models of suspensions: simulations are performed in the zero particle-inertia and zero fluid-inertia limits ($St \to 0$ and $Re \to 0$), and include relevant hydrodynamic interactions and a short-range repulsive potential. The critical innovation is that, besides this purely hydrodynamic basis, it adds frictional contacts between solid particles. This model can be used to simulate sheared suspensions over a range of volume fractions, from mildly dense, where the short range hydrodynamic interactions dominate, to the jamming point, where contact forces dominate.

The effect of adding frictional contacts is striking at large volume fractions: tangential forces due to friction restrict microscopic rearrangements in the system, resulting in a large shear stress. The number of contacts created during the flow is the result of a competition between applied shear forces and the short-range repulsive forces. Therefore, alongside the

contactless (hence frictionless) rheology at low shear rates a new contact dominated frictional rheology appears at high shear rates. Shear thickening is then simply the transition from the contactless rheology to the contact dominated rheology with increasing shear stress (and shear rate). The strongest evidence that this stress-induced friction scenario is correct is the ability of our model to reproduce shear thickening, including its discontinuous form, and its volume-fraction dependence. Therefore, we conclude that friction is a key element for shear thickening.

Physically, the two qualitatively different behaviors, CST and DST, can be explained in this scenario as stemming from the level of contrast that exists between the two rheologies, as suggested by Wyart and Cates [2014]. Recalling that the number of frictional contacts essentially depends on the applied shear stress, and noting that the viscosity interpolates between the two rheologies according to the number of frictional contacts, we see that we can write a direct relation $\eta(\sigma)$ between the viscosity and the applied stress. If the difference between the two rheologies is small —i.e., $\eta(\sigma \to \infty) - \eta(\sigma \to 0)$ is small— the curve $\eta(\sigma)$ is a sufficiently mildly increasing function such that $\dot{\gamma} = \sigma/\eta(\sigma)$ is also an increasing function of σ; this corresponds to a single-valued curve $\sigma(\dot{\gamma})$, and thus to CST. But if the difference $\eta(\sigma \to \infty) - \eta(\sigma \to 0)$ becomes too large, $\eta(\sigma)$ increases faster than σ in some interval, which means that $\dot{\gamma}(\sigma)$ is a decreasing function in this same interval. This corresponds to a multivalued curve $\sigma(\dot{\gamma})$, which is unstable, and shows up experimentally as a discontinuous curve, i.e., DST.

An increasing difference $\eta(\sigma \to \infty) - \eta(\sigma \to 0)$ is naturally provided in our model by the fact that the frictional rheology diverges at a jamming volume fraction ϕ_{J}^{μ} that is smaller than the frictionless rheology jamming point ϕ_{J}^{0}. Then, at low volume fraction, the difference is small, but there must be a point ϕ below ϕ_{J}^{μ} where the difference becomes large enough to get a DST.

Though our model assumes non-Brownian suspensions, we may expect that the same mechanism explains shear thickening of Brownian colloidal suspensions. Indeed, the Brownian forces qualitatively play a role similar to the repulsive potential that we use in our ERM: at low shear stress, the Brownian forces are large enough to randomly open gaps between contacting particles, while at high shear stress this becomes much less likely. Friction would then develop in a very similar manner in a Brownian suspension.

ACKNOWLEDGMENTS

We would like to thank Mike Cates and Matthieu Wyart for the many discussions concerning our respective work. Our code makes use of the CHOLMOD library by Tim Davis (https://www.cise.ufl.edu/research/sparse/cholmod/). This research was supported in part by a grant of computer time from the City University of New York High Performance Computing Center under NSF Grants CNS-0855217, CNS-0958379, and ACI-1126113.

Appendix A: Hydrodynamic resistances

The hydrodynamic interactions arising from an imposed background flow and relative motions between nearby particles are given by

$$\begin{pmatrix} \boldsymbol{F}_{\mathrm{H}} \\ \boldsymbol{T}_{\mathrm{H}} \end{pmatrix} = -(\boldsymbol{R}_{\mathrm{Stokes}} + \boldsymbol{R}_{\mathrm{Lub}}) \cdot \begin{pmatrix} \boldsymbol{U} - \boldsymbol{U}^{\infty} \\ \boldsymbol{\Omega} - \boldsymbol{\Omega}^{\infty} \end{pmatrix} + \boldsymbol{R}'_{\mathrm{Lub}} : \boldsymbol{E}^{\infty}, \tag{A1}$$

where a diagonal matrix $\boldsymbol{R}_{\mathrm{Stokes}}$ comes from the (one-body) Stokes drag and sparse matrices $\boldsymbol{R}_{\mathrm{Lub}}$ and $\boldsymbol{R}'_{\mathrm{Lub}}$ come from the (two-body) lubrication.

Using the basic units $L_0 \equiv a$ for lengths, $U_0 \equiv L_0\dot{\gamma}$ for velocities, and $F_0 \equiv 6\pi\eta_0 L_0 U_0$ for forces, the elements of $\boldsymbol{R}_{\mathrm{Stokes}}$ give the Stokes drag through

$$\begin{pmatrix} \boldsymbol{F}^{(i)}_{\mathrm{Stokes}} \\ \boldsymbol{T}^{(i)}_{\mathrm{Stokes}} \end{pmatrix} = -\boldsymbol{R}^{(i,i)}_{\mathrm{Stokes}} \cdot \begin{pmatrix} \boldsymbol{U}^{(i)} - \boldsymbol{U}^{\infty}(\boldsymbol{r}^{(i)}) \\ \boldsymbol{\Omega}^{(i)} - \boldsymbol{\Omega}^{\infty} \end{pmatrix} = -\begin{pmatrix} \boldsymbol{U}^{(i)} - \boldsymbol{U}^{\infty}(\boldsymbol{r}^{(i)}) \\ (4/3)(\boldsymbol{\Omega}^{(i)} - \boldsymbol{\Omega}^{\infty}) \end{pmatrix}, \tag{A2}$$

while $\boldsymbol{R}_{\mathrm{Lub}}$ and $\boldsymbol{R}'_{\mathrm{Lub}}$ consist of off-diagonal blocks giving the lubrication forces and torques for a pair (i, j) through

$$\begin{pmatrix} \boldsymbol{F}^{(i,j)}_{\mathrm{H}} \\ \boldsymbol{F}^{(j,i)}_{\mathrm{H}} \\ \boldsymbol{T}^{(i,j)}_{\mathrm{H}} \\ \boldsymbol{T}^{(j,i)}_{\mathrm{H}} \end{pmatrix} = -\boldsymbol{R}^{(i,j)}_{\mathrm{Lub}} \cdot \begin{pmatrix} \boldsymbol{U}^{(i)} - \boldsymbol{U}^{\infty}(\boldsymbol{r}^{(i)}) \\ \boldsymbol{U}^{(j)} - \boldsymbol{U}^{\infty}(\boldsymbol{r}^{(j)}) \\ \boldsymbol{\Omega}^{(i)} - \boldsymbol{\Omega}^{\infty} \\ \boldsymbol{\Omega}^{(j)} - \boldsymbol{\Omega}^{\infty} \end{pmatrix} + \boldsymbol{R}'^{(i,j)}_{\mathrm{H}} : \begin{pmatrix} \boldsymbol{E}^{\infty} \\ \boldsymbol{E}^{\infty} \end{pmatrix}. \tag{A3}$$

Following the notation of Jeffrey and Onishi [1984], Jeffrey [1992], the matrices $\boldsymbol{R}^{(i,j)}_{\mathrm{Lub}}$ and $\boldsymbol{R}'^{(i,j)}_{\mathrm{Lub}}$ are obtained from the particle positions as (we give only the upper triangular part of the symmetric $\boldsymbol{R}^{(i,j)}_{\mathrm{Lub}}$):

$$\boldsymbol{R}^{(i,j)}_{\mathrm{Lub}} \equiv \begin{pmatrix} X^A_{ii}\,\mathrm{P}_{\boldsymbol{n}_{ij}} + Y^A_{ii}\,\mathrm{P}'_{\boldsymbol{n}_{ij}} & X^A_{ij}\,\mathrm{P}_{\boldsymbol{n}_{ij}} + Y^A_{ij}\,\mathrm{P}'_{\boldsymbol{n}_{ij}} & Y^B_{ii}\,\mathrm{P}^{\mathrm{r}}_{\boldsymbol{n}_{ij}} & Y^B_{ji}\,\mathrm{P}^{\mathrm{r}}_{\boldsymbol{n}_{ij}} \\ \cdot & X^A_{jj}\,\mathrm{P}_{\boldsymbol{n}_{ij}} + Y^A_{jj}\,\mathrm{P}'_{\boldsymbol{n}_{ij}} & Y^B_{ij}\,\mathrm{P}^{\mathrm{r}}_{\boldsymbol{n}_{ij}} & Y^B_{jj}\,\mathrm{P}^{\mathrm{r}}_{\boldsymbol{n}_{ij}} \\ \cdot & \cdot & Y^C_{ii}\,\mathrm{P}'_{\boldsymbol{n}_{ij}} & Y^C_{ij}\,\mathrm{P}'_{\boldsymbol{n}_{ij}} \\ \cdot & \cdot & \cdot & Y^C_{jj}\,\mathrm{P}'_{\boldsymbol{n}_{ij}} \end{pmatrix}, \tag{A4}$$

$$\boldsymbol{R}'^{(i,j)}_{\mathrm{Lub}} \equiv \begin{pmatrix} X^G_{ii}\,\mathrm{Q}_{\boldsymbol{n}_{ij}} + Y^G_{ii}\,\mathrm{Q}'_{\boldsymbol{n}_{ij}} & X^G_{ji}\,\mathrm{Q}_{\boldsymbol{n}_{ij}} + Y^G_{ji}\,\mathrm{Q}'_{\boldsymbol{n}_{ij}} \\ X^G_{ij}\,\mathrm{Q}_{\boldsymbol{n}_{ij}} + Y^G_{ij}\,\mathrm{Q}'_{\boldsymbol{n}_{ij}} & X^G_{jj}\,\mathrm{Q}_{\boldsymbol{n}_{ij}} + Y^G_{jj}\,\mathrm{Q}'_{\boldsymbol{n}_{ij}} \\ Y^H_{ii}\,\mathrm{Q}^{\mathrm{r}}_{\boldsymbol{n}_{ij}} & Y^H_{ji}\,\mathrm{Q}^{\mathrm{r}}_{\boldsymbol{n}_{ij}} \\ Y^H_{ij}\,\mathrm{Q}^{\mathrm{r}}_{\boldsymbol{n}_{ij}} & Y^H_{jj}\,\mathrm{Q}^{\mathrm{r}}_{\boldsymbol{n}_{ij}} \end{pmatrix}. \tag{A5}$$

In these expressions, we have introduced the normal projection operator $\mathrm{P}_{\boldsymbol{n}_{ij}} \equiv \boldsymbol{n}_{ij}\boldsymbol{n}_{ij}$, the tangential projection operator $\mathrm{P}'_{\boldsymbol{n}_{ij}} \equiv \boldsymbol{I} - \boldsymbol{n}_{ij}\boldsymbol{n}_{ij}$, and the "cross product" operator $\mathrm{P}^{\mathrm{r}}_{\boldsymbol{n}_{ij}}$ defined as $\mathrm{P}^{\mathrm{r}}_{\boldsymbol{n}_{ij}}\,\boldsymbol{q} \equiv \boldsymbol{n}_{ij} \times \boldsymbol{q}$. We also used the operators $\mathrm{Q}_{\boldsymbol{n}_{ij}}$, $\mathrm{Q}'_{\boldsymbol{n}_{ij}}$ and $\mathrm{Q}^{\mathrm{r}}_{\boldsymbol{n}_{ij}}$ defined for an arbitrary matrix $\boldsymbol{M}$ as:

$$\begin{aligned} \mathrm{Q}_{\boldsymbol{n}_{ij}}\,\boldsymbol{M} &\equiv \left(\boldsymbol{M} : \boldsymbol{n}_{ij}\boldsymbol{n}_{ij} - \frac{1}{3}\,\mathrm{Tr}\,\boldsymbol{M}\right)\boldsymbol{n}_{ij}, \\ \mathrm{Q}'_{\boldsymbol{n}_{ij}}\,\boldsymbol{M} &\equiv \left(\boldsymbol{M} + \boldsymbol{M}^{\mathrm{T}}\right) \cdot \boldsymbol{n}_{ij} - 2(\boldsymbol{M} : \boldsymbol{n}_{ij}\boldsymbol{n}_{ij})\boldsymbol{n}_{ij}, \\ \mathrm{Q}^{\mathrm{r}}_{\boldsymbol{n}_{ij}}\,\boldsymbol{M} &\equiv 2\boldsymbol{n}_{ij} \times \left[\left(\boldsymbol{M} + \boldsymbol{M}^{\mathrm{T}}\right) \cdot \boldsymbol{n}_{ij}\right]. \end{aligned} \tag{A6}$$

The scalar coefficients X and Y have an explicit dependence on the non-dimensional interparticle gap $h^{(i,j)} \equiv 2(r^{(i,j)} - a_i - a_j)/(a_i + a_j)$, and we use only the terms of leading order:

$$X \equiv g^X \frac{1}{h^{(i,j)} + \delta}, \quad Y \equiv g^Y \log \frac{1}{h^{(i,j)} + \delta}. \tag{A7}$$

With $\lambda \equiv a_j/a_i$, the coefficients g^X and g^Y appearing in $\boldsymbol{R}_{\rm Lub}^{(i,j)}$ are written

$$
\begin{aligned}
g^{X_{ii}^A}(\lambda) &= 2a_i \frac{\lambda^2}{(1+\lambda)^3}, & g^{X_{jj}^A}(\lambda) &= \lambda g^{X_{ii}^A}(\lambda^{-1}),\\
g^{X_{ij}^A}(\lambda) &= -2(a_i+a_j)\frac{\lambda^2}{(1+\lambda)^4}, & g^{X_{ji}^A}(\lambda) &= g^{X_{ij}^A}(\lambda^{-1}) = g^{X_{ij}^A}(\lambda),\\
g^{Y_{ii}^A}(\lambda) &= \frac{4a_i}{15}\frac{\lambda(2+\lambda+2\lambda^2)}{(1+\lambda)^3}, & g^{Y_{jj}^A}(\lambda) &= \lambda g^{Y_{ii}^A}(\lambda^{-1}),\\
g^{Y_{ij}^A}(\lambda) &= -\frac{4(a_i+a_j)}{15}\frac{\lambda(2+\lambda+2\lambda^2)}{(1+\lambda)^4}, & g^{Y_{ji}^A}(\lambda) &= g^{Y_{ij}^A}(\lambda^{-1}) = g^{Y_{ij}^A}(\lambda),\\
g^{Y_{ii}^B}(\lambda) &= -\frac{2a_i^2}{15}\frac{\lambda(4+\lambda)}{(1+\lambda)^2}, & g^{Y_{jj}^B}(\lambda) &= -\lambda^2 g^{Y_{ii}^B}(\lambda^{-1}),\\
g^{Y_{ij}^B}(\lambda) &= \frac{2(a_i+a_j)^2}{15}\frac{\lambda(4+\lambda)}{(1+\lambda)^4}, & g^{Y_{ji}^B}(\lambda) &= -g^{Y_{ij}^B}(\lambda^{-1}),\\
g^{Y_{ii}^C}(\lambda) &= \frac{8a_i^3}{15}\frac{\lambda}{1+\lambda}, & g^{Y_{jj}^C}(\lambda) &= \lambda^3 g^{Y_{ii}^C}(\lambda^{-1}) = \lambda^2 g^{Y_{ii}^C}(\lambda),\\
g^{Y_{ij}^C}(\lambda) &= \frac{2(a_i+a_j)^3}{15}\frac{\lambda^2}{(1+\lambda)^4}, & g^{Y_{ji}^C}(\lambda) &= g^{Y_{ij}^C}(\lambda^{-1}) = g^{Y_{ij}^C}(\lambda).
\end{aligned}
\tag{A8}
$$

Similarly, the terms appearing in $\boldsymbol{R}_{\rm Lub}^{\prime(i,j)}$ are

$$
\begin{aligned}
g^{X_{ii}^G}(\lambda) &= 2a_i^2 \frac{\lambda^2}{(1+\lambda)^3}, & g^{X_{jj}^G}(\lambda) &= -\lambda^2 g^{X_{ii}^G}(\lambda^{-1}),\\
g^{X_{ij}^G}(\lambda) &= -2(a_i+a_j)^2\frac{\lambda^2}{(1+\lambda)^5}, & g^{X_{ji}^G}(\lambda) &= -g^{X_{ij}^G}(\lambda^{-1}),\\
g^{Y_{ii}^G}(\lambda) &= \frac{a_i^2}{15}\frac{4\lambda-\lambda^2+7\lambda^3}{(1+\lambda)^3}, & g^{Y_{jj}^G}(\lambda) &= -\lambda^2 g^{Y_{ii}^G}(\lambda^{-1}),\\
g^{Y_{ij}^G}(\lambda) &= -\frac{(a_i+a_j)^2}{15}\frac{4\lambda-\lambda^2+7\lambda^3}{(1+\lambda)^5}, & g^{Y_{ji}^G}(\lambda) &= -g^{Y_{ij}^G}(\lambda^{-1}),\\
g^{Y_{ii}^H}(\lambda) &= \frac{2a_i^3}{15}\frac{2\lambda-\lambda^2}{(1+\lambda)^2}, & g^{Y_{jj}^H}(\lambda) &= \lambda^3 g^{Y_{ii}^G}(\lambda^{-1}),\\
g^{Y_{ij}^H}(\lambda) &= \frac{(a_i+a_j)^3}{15}\frac{\lambda^2+7\lambda^3}{(1+\lambda)^5}, & g^{Y_{ji}^H}(\lambda) &= g^{Y_{ij}^H}(\lambda^{-1}).
\end{aligned}
\tag{A9}
$$

Appendix B: Contact model

1. Tuning the spring constants

Our objective is to study the rheology of hard-sphere suspensions. We have no way to mimic rigorously hard spheres by using a contact model with springs. To provide the best approximation to hard spheres, the elastic constants appearing in the contact model must satisfy a simple constraint: they should be large enough to generate as little geometric

overlap as possible between the particles. (An equivalent way to state this is through the requirement that the contact based non-dimensionalized shear rate $6\pi\eta_0 a\dot{\gamma}/k_\mathrm{n} \ll 1$ introduced in section II B 1 is sufficiently small.)

We therefore set a criterion for the overlap: the largest overlap between any two particles during the simulation should not be larger than h_max (5 % of the particle radius in this simulation). As the overlap $|h|$ depends on the shear stress, an estimate being $\langle|h|\rangle \sim (1/k_\mathrm{n})\sigma(\phi,\dot{\gamma})a^2$, the spring constant has to be tuned for every ϕ and $\dot{\gamma}$ so that $\max(|h|) < h_\mathrm{max}$. We introduce a similar criterion for the tangential spring stretch mimicking static friction: we pick $k_\mathrm{t}(\phi,\dot{\gamma})$ so that ξ is smaller than 5 % of the particle radius. We detail below how we fulfill these two conditions and retain hard-sphere like behavior in our simulation.

For a given ϕ, the largest stress is obtained in the high shear-rate limit. Hence, we start by determining high shear-rate spring constants $\big(k_\mathrm{n}^*(\phi), k_\mathrm{t}^*(\phi)\big)$ by running pre-simulations at $\dot{\gamma} \to \infty$, where these values are regularly updated with a certain interval until the criteria on the overlap and the tangential spring stretch are fulfilled.

Second, a trivial shear-rate dependence comes in if the contact model introduces a force scale in addition to the hydrodynamic one. Avoiding this requires to picking the shear rate dependence of $k_\mathrm{n}(\phi,\dot{\gamma})$ and $k_\mathrm{n}(\phi,\dot{\gamma})$ by scaling these parameters with the shear rate; i.e., $k_\mathrm{n}(\phi,\dot{\gamma}) = \dot{\gamma}k_\mathrm{n}^*(\phi)$ and $k_\mathrm{t}(\phi,\dot{\gamma}) = \dot{\gamma}k_\mathrm{t}^*(\phi)$. With this scaling, there is no competition between hydrodynamic and contact forces, as they are proportional, so an additional explicit force scale (as the one in section II B) is required to have a shear-rate dependence in our simulation. Also notice that as the high shear-rate limit is always the largest viscosity at a given ϕ, with this choice of scaling $k_\mathrm{n}(\phi,\dot{\gamma})$ and $k_\mathrm{t}(\phi,\dot{\gamma})$ always fulfill the criteria we set for the overlap and tangential spring stretch.

2. Combining the overdamped dynamics and the contact model

In this appendix we present a slightly more general contact model than the one presented in the main text. While the contact model may not deserve a lengthy description in itself, immersing an orthodox contact model in overdamped dynamics leads to non-trivial difficulties, which justifies our use of a simpler version of the model.

A more general stick/slide friction model using springs and dashpots is the following [Cundall and Strack 1979, Luding 2008]:

$$\begin{aligned}
\boldsymbol{F}_\mathrm{C,nor}^{(i,j)} &= k_\mathrm{n} h^{(i,j)} \boldsymbol{n}_{ij} + \gamma_\mathrm{n} \boldsymbol{U}_\mathrm{n}^{(i,j)}, \\
\boldsymbol{F}_\mathrm{C,tan}^{(i,j)} &= k_\mathrm{t} \boldsymbol{\xi}^{(i,j)} + \gamma_\mathrm{t} \boldsymbol{U}_\mathrm{t}^{(i,j)}, \\
\boldsymbol{T}_\mathrm{C,tan}^{(i,j)} &= a_i \boldsymbol{n}_{ij} \times \boldsymbol{F}_\mathrm{C,tan}^{(i,j)},
\end{aligned} \tag{B1}$$

These forces must fulfill Coulomb's law of friction: $|\boldsymbol{F}_\mathrm{C,tan}^{(i,j)}| \leq \mu |\boldsymbol{F}_\mathrm{C,nor}^{(i,j)}|$. In the above expression, k_n and k_t are respectively the normal and tangential spring constants, and γ_n and γ_t are the damping constants. The normal and tangential relative velocities between two particles i and j are $\boldsymbol{U}_\mathrm{n}^{(i,j)} \equiv \mathrm{P}_{\boldsymbol{n}_{ij}}\big(\boldsymbol{U}^{(j)} - \boldsymbol{U}^{(i)}\big)$ and $\boldsymbol{U}_\mathrm{t}^{(i,j)} \equiv \mathrm{P}'_{\boldsymbol{n}_{ij}}\Big[\boldsymbol{U}^{(j)} - \boldsymbol{U}^{(i)} - \big(a_i\boldsymbol{\Omega}^{(i)} + a_j\boldsymbol{\Omega}^{(j)}\big) \times \boldsymbol{n}_{ij}\Big]$. Finally, the quantity $\boldsymbol{\xi}^{(i,j)}$ is the tangential spring stretch.

The computation of the tangential spring stretch $\boldsymbol{\xi}^{(i,j)}$, described in the following, requires some care, as we have to impose Coulomb's law, which is made difficult by the overdamped dynamics. At the time t_0 at which the contact (i,j) is created, we set an unstretched

tangential spring $\boldsymbol{\xi}^{(i,j)}(t_0) = \mathbf{0}$. At any further time step t in the simulation, the tangential stretch $\boldsymbol{\xi}^{(i,j)}(t)$ is incremented according to the value of a "test" force, $\boldsymbol{F}^{\prime(i,j)}_{\mathrm{C,tan}}(t + \mathrm{d}t) = k_\mathrm{t}\boldsymbol{\xi}^{\prime(i,j)}(t+\mathrm{d}t)+\gamma_\mathrm{t}\boldsymbol{U}^{(i,j)}_\mathrm{t}(t+dt)$ with the tentative update of stretch $\boldsymbol{\xi}^{\prime(i,j)}(t+\mathrm{d}t) = \boldsymbol{\xi}^{(i,j)}(t)+\boldsymbol{U}^{(i,j)}_\mathrm{t}(t)\mathrm{d}t$. If $\big|\boldsymbol{F}^{\prime(i,j)}_{\mathrm{C,tan}}(t+\mathrm{d}t)\big| \leq \mu\big|\boldsymbol{F}^{(i,j)}_{\mathrm{C,nor}}(t+\mathrm{d}t)\big|$, the contact is in a static friction state and we update the spring stretch as $\boldsymbol{\xi}^{(i,j)}(t+\mathrm{d}t) = \boldsymbol{\xi}^{\prime(i,j)}(t+\mathrm{d}t)$ and the corresponding tangential force is $\boldsymbol{F}^{(i,j)}_{\mathrm{C,tan}}(t+\mathrm{d}t) = \boldsymbol{F}^{\prime(i,j)}_{\mathrm{C,tan}}(t+\mathrm{d}t)$. However, if $\big|\boldsymbol{F}^{\prime(i,j)}_{\mathrm{C,tan}}(t+\mathrm{d}t)\big| > \mu\big|\boldsymbol{F}^{(i,j)}_{\mathrm{C,nor}}(t+\mathrm{d}t)\big|$, the contact is in sliding state and the spring is updated as $\boldsymbol{\xi}^{(i,j)}(t+\mathrm{d}t) = (1/k_\mathrm{t})\Big(\mu\big|\boldsymbol{F}^{(i,j)}_{\mathrm{C,nor}}(t+\mathrm{d}t)\big|\boldsymbol{t} - \gamma_\mathrm{t}\boldsymbol{U}^{(i,j)}_\mathrm{t}(t)\Big)$, where the direction is the same as the test force, i.e., $\boldsymbol{t} \equiv \boldsymbol{F}^{\prime(i,j)}_{\mathrm{C,tan}}(t+\mathrm{d}t)/\big|\boldsymbol{F}^{\prime(i,j)}_{\mathrm{C,tan}}(t+\mathrm{d}t)\big|$. *Assuming that the velocities are continuous in time*, this ensures that the contact force will at most weakly violate the Coulomb friction law for the next time step, as the force effectively used in the equation of motion will be $\boldsymbol{F}^{(i,j)}_{\mathrm{C,tan}}(t+\mathrm{d}t) = k_\mathrm{t}\boldsymbol{\xi}^{(i,j)}(t+\mathrm{d}t)+\gamma_\mathrm{t}\boldsymbol{U}^{(i,j)}_\mathrm{t}(t+\mathrm{d}t) = \mu\big|\boldsymbol{F}^{(i,j)}_{\mathrm{C,nor}}(t+\mathrm{d}t)\big|\boldsymbol{t}+\gamma_\mathrm{t}\dot{\boldsymbol{U}}^{(i,j)}_\mathrm{t}\mathrm{d}t$, so that $\big|\boldsymbol{F}^{(i,j)}_{\mathrm{C,tan}}(t+\mathrm{d}t)\big| = \mu\big|\boldsymbol{F}^{(i,j)}_{\mathrm{C,nor}}(t+\mathrm{d}t)\big| + \mathcal{O}(\mathrm{d}t)$.

Of course, if velocities happen to be discontinuous, the Coulomb's law might be violated significantly, and this is the source of one problem when merging this contact model with the hydrodynamic interaction model. Indeed, when contacts are created and destroyed during the flow (which happens very frequently), the overall resistance matrix changes discontinuously, as dashpots are switched on and off. But, as other position-dependent forces are continuous in time, solving the force balance equation will lead to a discontinuity in velocities when a contact forms or breaks. This, in turn, leads to large violations of Coulomb's law, and hence to numerical instabilities where contacts keep switching between static and dynamic cases at every time step.

Another problem occurs when a contact forms (i.e., $\boldsymbol{\xi}^{(i,j)}(t) = 0$): as by definition the normal load on the new contact $\big|\boldsymbol{F}^{(i,j)}_{\mathrm{C,nor}}(t + \mathrm{d}t)\big|$ vanishes (or is very small in the simulation owing to the finite time-step), the finite test force $\boldsymbol{F}^{\prime(i,j)}_{\mathrm{C,tan}}(t + \mathrm{d}t) \simeq \gamma_\mathrm{t}\boldsymbol{U}^{(i,j)}_\mathrm{t}(t)$ will lead to an immediate rescaling of the tangential spring as $\boldsymbol{\xi}^{(i,j)}(t + \mathrm{d}t) \simeq -(\gamma_\mathrm{t}/k_\mathrm{t})\boldsymbol{U}^{(i,j)}_\mathrm{t}(t)$; i.e., an entirely new finite force appears right at contact time.

These two problems actually also exist in simulations of dry granular matter [Walton 1993a], but they are more acute with an overdamped dynamics because of the direct relation between forces and velocities. In this case, any discontinuity in forces or velocities rapidly causes numerical instabilities. A solution is to use a continuously varying damping $\gamma_\mathrm{t}(h_{ij})$ such that $\gamma_\mathrm{t}(h_{ij} = 0) = 0$, which ensures the continuity of forces and velocities [Walton 1993b] at the cost of increased complexity of the model. The solution that we prefer using here is to eliminate of the tangential dashpot by setting $\gamma_\mathrm{t} = 0$. In any case, this dashpot has no physical significance, and it is only used in granular matter simulations as an efficient numerical stabilizer. In our already overdamped context, as long as the hydrodynamic resistance associated with tangential motion is not too small, we do not need such an extra resistive stabilizer, and we do not face any major difficulty by simply dropping this dashpot.

We can quantify this assertion by looking at the relaxation times associated with a contact. Both normal and tangential contacts have relaxation times. For the normal part, it is the one of a spring and dashpot system, $\tau_\mathrm{n} = \gamma_\mathrm{n}/k_\mathrm{n}$. For the tangential part, the damping is provided by the hydrodynamic resistance, which we here simply denote $\gamma^\mathrm{H}_\mathrm{t}$, so that $\tau_\mathrm{t} = \gamma^\mathrm{H}_\mathrm{t}/k_\mathrm{t}$. On the one hand, in order to have a stable numerical scheme, one should chose these relaxation times large enough compared to the time step τ_n, $\tau_\mathrm{t} \gg \mathrm{d}t$. On the other hand, contacts of hard spheres should react instantaneously to any external load, so physics

imposes relaxation times smaller than other typical times τ_{n}, $\tau_{\mathrm{t}} \ll 1/\dot{\gamma}$. For the normal part of the contact, we are free to choose the damping γ_{n} to achieve this. For the tangential part however, we check that those scale separations are verified.

H. A. Barnes, "Shear-thickening ("dilatancy") in suspensions of nonaggregating solid particles dispersed in newtonian liquids," J. Rheol. **33**, 329–366 (1989).

E. Brown and H. M. Jaeger, "Shear thickening in concentrated suspensions: phenomenology, mechanisms, and relations to jamming," Rep. Prog. Phys. (2014).

R. V. Williamson, "Some unusual properties of colloidal dispersions," J. Phys. Chem. **35**, 354–359 (1930).

R. V. Williamson and W. W. Hecker, "Some properties of dispersions of the quicksand type," Ind. Eng. Chem. **23**, 667–670 (1931).

H. Freundlich and H. L. Roder, "Dilatancy and its relation to thixotropy," Trans. Faraday Soc. **34**, 308–316 (1938).

M. E. Fagan and C. F. Zukoski, "The rheology of charge stabilized silica suspensions," J. Rheol. **41**, 373–397 (1997).

W. H. Boersma, J. Laven, and H. N. Stein, "Shear thickening (dilatancy) in concentrated dispersions," AIChE J. **36**, 321–332 (1990).

R. L. Hoffman, "Discontinuous and dilatant viscosity behavior in concentrated suspensions. i. observation of a flow instability," Trans. Soc. Rheol. **16**, 155–173 (1972).

P. D'Haene, Jan Mewis, and G. G. Fuller, "Scattering dichroism measurements of flow-induced structure of a shear thickening suspension," J. Colloid Interface Sci. **156**, 350–358 (1993).

Vincent T. O'Brien and Michael E. Mackay, "Stress components and shear thickening of concentrated hard sphere suspensions," Langmuir **16**, 7931–7938 (2000).

A. B. Metzner and M. Whitlock, "Flow behavior of concentrated (dilatant) suspensions," Trans. Soc. Rheol. , 239–253 (1958).

Jonathan W. Bender and Norman J. Wagner, "Optical measurement of the contributions of colloidal forces to the rheology of concentrated suspensions," J. Colloid Interface Sci. **172**, 171–184 (1995).

J. Bender and N. J. Wagner, "Reversible shear thickening in monodisperse and bidisperse colloidal dispersions," J. Rheol. **40**, 899–916 (1996).

B. J. Maranzano and N. J. Wagner, "The effects of particle size on reversible shear thickening of concentrated colloidal dispersions," J. Chem. Phys. **114**, 10514–527 (2001a).

B. J. Maranzano and N. J. Wagner, "The effects of interparticle interactions and particle size on reversible shear thickening: Hard-sphere colloidal dispersions," J. Rheol. **45**, 1205–1222 (2001b).

B. J. Maranzano and N. J. Wagner, "Flow-small angle neutron scattering measurements of colloidal dispersion microstructure evolution through the shear thickening transition," J. Chem. Phys. **117**, 10291–302 (2002).

William J. Frith, P. d'Haene, Richard Buscall, and Jan Mewis, "Shear thickening in model suspensions of sterically stabilized particles," J. Rheol. **40**, 531–548 (1996).

D. Lootens, P. Hébraud, E. Lécolier, and H. Van Damme, "Coagulation, rhéofluidification et rhéoépaississement dans les coulis de ciment," Oil Gas Sci. Technol.- Rev. IFP. **59**, 31–40 (2004).

D. Lootens, Henri van Damme, Y. Hémar, and P. Hébraud, "Dilatant flow of concentrated suspensions of rough particles," Phys. Rev. Lett. **95**, 268302 (2005).

Ryan J. Larsen, Jin-Woong Kim, Charles F. Zukoski, and David A. Weitz, "Elasticity of dilatant

particle suspensions during flow," Phys. Rev. E **81**, 011502 (2010).
E. Bertrand, J. Bibette, and V. Schmitt, "From shear thickening to shear-induced jamming," Phys. Rev. E **66**, 060401 (2002).
E. Brown and H. M. Jaeger, "Dynamic jamming point for shear thickening suspensions," Phys. Rev. Lett. **103**, 086001 (2009).
E. Brown and H. M. Jaeger, "The role of dilation and confining stresses in shear thickening of dense suspensions," J. Rheol. **56**, 875–923 (2012).
Abdoulaye Fall, Anaël Lemaître, François Bertrand, Daniel Bonn, and Guillaume Ovarlez, "Shear thickening and migration in granular suspensions," Phys. Rev. Lett. **105**, 268303 (2010).
Anaël Lemaître, Jean-Noël Roux, and François Chevoir, "What do dry granular flows tell us about dense non-brownian suspension rheology?" Rheol. Acta **48**, 925–942 (2009).
Martin Trulsson, Bruno Andreotti, and Philippe Claudin, "Transition from the viscous to inertial regime in dense suspensions," Phys. Rev. Lett. **109**, 118305 (2012).
Nicolas Fernandez, Roman Mani, David Rinaldi, Dirk Kadau, Martin Mosquet, Hélène Lombois-Burger, Juliette Cayer-Barrioz, Hans J. Herrmann, Nicholas D. Spencer, and Lucio Isa, "Microscopic mechanism for shear thickening of non-brownian suspensions," Phys. Rev. Lett. **111**, 108301 (2013).
R. A. Bagnold, "Experiments on a gravity-free dispersion of large solid spheres in a newtonian fluid under shear," Proc. R. Soc. Lond. A **225**, 49–63 (1954).
J. F. Brady and G. Bossis, "The rheology of concentrated suspensions of spheres in simple shear flow by numerical simulation," J. Fluid Mech. **155**, 105–129 (1985).
J. R. Melrose and R. C. Ball, ""contact networks" in continuously shear thickening colloids," J. Rheol. **48**, 961–978 (2004a).
N. J. Wagner and J. F. Brady, "Shear thickening in colloidal dispersions," Phys. Today **62**, 27–32 (2009).
J. F. Brady and G. Bossis, "Stokesian dynamics," Ann. Rev. Fluid Mech. **20**, 111–157 (1988).
Georges Bossis and John F. Brady, "The rheology of brownian suspensions," J. Chem. Phys. **91**, 1866–1874 (1989).
T. N. Phung, J. F. Brady, and G. Bossis, "Stokesian dynamics simulation of brownian suspensions," J. Fluid Mech. **313**, 181–207 (1996).
D. R. Foss and J. F. Brady, "Structure, diffusion and rheology of brownian suspensions by stokesian dynamics simulation," J. Fluid Mech. **407**, 167–200 (2000).
J. R. Melrose and R. C. Ball, "Continuous shear thickening transitions in model concentrated colloids–the role of interparticle forces," J. Rheol. **48**, 937–960 (2004b).
François. Boyer, Élisabeth Guazzelli, and Olivier Pouliquen, "Unifying suspension and granular rheology," Phys. Rev. Lett. **107**, 188301 (2011).
Angélique Deboeuf, Georges Gauthier, Jérôme Martin, Yevgeny Yurkovetsky, and Jeffrey F. Morris, "Particle pressure in a sheared suspension: A bridge from osmosis to granular dilatancy," Phys. Rev. Lett. **102**, 108301 (2009).
Frédéric da Cruz, Sacha Emam, Michaël Prochnow, Jean-Noël Roux, and François Chevoir, "Rheophysics of dense granular materials: Discrete simulation of plane shear flows," Phys. Rev. E **72**, 021309 (2005).
Yoël Forterre and Olivier Pouliquen, "Flows of dense granular media," Annu. Rev. Fluid Mech. **40**, 1–24 (2008).
Edan Lerner, Gustavo Düring, and Matthieu Wyart, "A unified framework for non-brownian suspension flows and soft amorphous solids," Proc. Natl. Acad. Sci. USA **109**, 4798–4803 (2012).

M. E. Cates, J. P. Wittmer, J.-P. Bouchaud, and P. Claudin, "Jamming, force chains, and fragile matter," Phys. Rev. Lett. **81**, 1841–1844 (1998).
Didier Lootens, Henri Van Damme, and Pascal Hébraud, "Giant stress fluctuations at the jamming transition," Phys. Rev. Lett. **90**, 178301 (2003).
Pascal Hébraud and Didier Lootens, "Concentrated suspensions under flow: shear-thickening and jamming," Mod. Phys. Lett. B **19**, 613–624 (2005).
Ryohei Seto, Romain Mari, Jeffrey F. Morris, and Morton M. Denn, "Discontinuous shear thickening of frictional hard-sphere suspensions," Phys. Rev. Lett. **111**, 218301 (2013).
Chaoming Song, Ping Wang, and Hernán A Makse, "A phase diagram for jammed matter," Nature **453**, 629–632 (2008).
Claus Heussinger, "Shear thickening in granular suspensions: inter-particle friction and dynamically correlated clusters," Phys. Rev. E **88**, 050201(R) (2013).
Robert H Davis, "Effects of surface roughness on a sphere sedimenting through a dilute suspension of neutrally buoyant spheres," Physics of Fluids A: Fluid Dynamics **4**, 2607 (1992).
Y. Zhao and R. H. Davis, "Interaction of two touching spheres in a viscous fluid," Chem. Eng. Sci. **57**, 1997–2006 (2002).
Frédéric Blanc, François Peters, and Elisabeth Lemaire, "Experimental signature of the pair trajectories of rough spheres in the shear-induced microstructure in noncolloidal suspensions," Phys. Rev. Lett. **107**, 208302 (2011).
R. C. Ball and J. R. Melrose, "A simulation technique for many spheres in quasi-static motion under frame-invariant pair drag and brownian forces," Physica A **247**, 444–472 (1997).
D. J. Jeffrey and Y. Onishi, "Calculation of the resistance and mobility functions for two unequal rigid spheres in low-reynolds-number flow," J. Fluid Mech. **139**, 261–290 (1984).
D. J. Jeffrey, "The calculation of the low reynolds number resistance functions for two unequal spheres," Phys. Fluids A **4**, 16–29 (1992).
R. C. Ball and J. R. Melrose, "Lubrication breakdown in hydrodynamic simulations of concentrated colloids," Adv. Colloid Interface Sci. **59**, 19–30 (1995).
Chih-Ming Ho and Yu-Chong Tai, "Micro-electro-mechanical-systems (mems) and fluid flows," Annu. Rev. Fluid Mech. **30**, 579–612 (1998).
P. A. Cundall and O. D. L. Strack, "A discrete numerical model for granular assemblies," Geotechnique **29**, 47–65 (1979).
S. Luding, "Cohesive, frictional powders: contact models for tension," Granular Matter **10**, 235–246 (2008).
J. N. Israelachvili, *Intermolecular and surface forces* (Academic Press, 2011).
G. K. Batchelor, "The stress system in a suspension of force-free particles," J. Fluid Mech. **41**, 545–570 (1970).
Yevgeny Yurkovetsky and Jeffrey F. Morris, "Particle pressure in sheared brownian suspensions," J. Rheol. **52**, 141–164 (2008).
A. W. Lees and S. F. Edwards, "The computer study of transport processes under extreme conditions," J. Phys. C. **5**, 1921 (1972).
Michio Otsuki and Hisao Hayakawa, "Critical scaling near jamming transition for frictional granular particles," Phys. Rev. E **83**, 051301 (2011).
W. H. Boersma, P. J. M. Baets, J. Laven, and H. N. Stein, "Time-dependent behavior and wall slip in concentrated shear thickening dispersions," J. Rheol. **35**, 1093–1120 (1991).
Matthieu Wyart and Michael E. Cates, "Discontinuous shear thickening without inertia in dense non-brownian suspensions," Phys. Rev. Lett. **112**, 098302 (2014).

M. Lee, M. Alcoutlabi, J. J. Magda, C. Dibble, M. J. Solomon, X. Shi, and G. B. McKenna, "The effect of the shear-thickening transition of model colloidal spheres on the sign of n1 and on the radial pressure profile in torsional shear flows," J. Rheol. **50**, 293–311 (2006).
Étienne Couturier, François Boyer, Olivier Pouliquen, and Élisabeth Guazzelli, "Suspensions in a tilted trough: second normal stress difference," J. Fluid Mech. **686**, 26 (2011).
T Dbouk, L. Lobry, and E. Lemaire, "Normal stresses in concentrated non-brownian suspensions," J. Fluid Mech. **715**, 239–272 (2013).
Isidro E. Zarraga, Davide A. Hill, and David T. Leighton, "The characterization of the total stress of concentrated suspensions of noncolloidal spheres in newtonian fluids," J. Rheol. **44**, 185–220 (2000).
Anugrah Singh and Prabhu R. Nott, "Experimental measurements of the normal stresses in sheared stokesian suspensions," J. Fluid Mech. **490**, 293–320 (2003).
S.-C. Dai, E. Bertevas, F. Qi, and R. I. Tanner, "Viscometric functions for noncolloidal sphere suspensions with newtonian matrices," J. Rheol. **57**, 493–510 (2013).
R. L. Hoffman, "Discontinuous and dilatant viscosity behavior in concentrated suspensions. ii. theory and experimental tests," J. Colloid Interface Sci. **46**, 491–506 (1974).
R. L. Hoffman, "Explanations for the cause of shear thickening in concentrated colloidal suspensions," J. Rheol. **42**, 111–123 (1998).
Hiroshi Watanabe, Ming-Long Yao, Kunihiro Osaki, Toshiyuki Shikata, Hirokazu Niwa, and Yotaro Morishima, "Nonlinear rheology of a concentrated spherical silica suspension:," Rheol. Acta **36**, 524–533 (1997).
H. Watanabe, Ming-Long Yao, Kunihiro Osaki, Toshiyuki Shikata, Hirokazu Niwa, Yotaro Morishima, Nitash P. Balsara, and Hao Wang, "Nonlinear rheology and flow-induced structure in a concentrated spherical silica suspension," Rheol. Acta **37**, 1–6 (1998).
Maurice C. Newstein, Hao Wang, Nitash P. Balsara, Amy A. Lefebvre, Yitzhak Shnidman, Hiroshi Watanabe, Kunihiro Osaki, Toshiyuki Shikata, Hirokazu Niwa, and Yotaro Morishima, "Microstructural changes in a colloidal liquid in the shear thinning and shear thickening regimes," J. Chem. Phys. **111**, 4827–4838 (1999).
Xiang Cheng, Jonathan H. McCoy, Jacob N. Israelachvili, and Itai Cohen, "Imaging the microscopic structure of shear thinning and thickening colloidal suspensions," Science **333**, 1276–1279 (2011).
H. M. Laun, R. Bung, S. Hess, W. Loose, O. Hess, K. Hahn, E. Hädicke, R. Hingmann, F. Schmidt, and P. Lindnerm, "Rheological and small angle neutron scattering investigation of shear-induced particle structures of concentrated polymer dispersions submitted to plane poiseuille and couette flow," J. Rheol. **36**, 743–787 (1992).
Sandeep D. Kulkarni and Jeffrey F. Morris, "Ordering transition and structural evolution under shear in brownian suspensions," J. Rheol. **53**, 417–439 (2009).
Dapeng Bi, J. Zhang, B. Chakraborty, and R. P. Behringer, "Jamming by shear," Nature **480**, 355–358 (2011).
Otis R Walton, "Numerical simulation of inelastic, frictional particle-particle interactions," (Butterworth-Heinemann, 1993) Chap. 25, pp. 884–911.
Otis R. Walton, "Numerical simulation of inclined chute flows of monodisperse, inelastic, frictional spheres," Mechanics of Materials **16**, 239–247 (1993b).